A one-dimensional Chandrasekhar-mass delayed-detonation model for the broad-lined Type Ia supernova 2002bo

Stéphane Blondin,[1][*] Luc Dessart[2] and D. John Hillier[3]

[1]*Aix Marseille Université, CNRS, LAM (Laboratoire d'Astrophysique de Marseille), UMR 7326, F-13388 Marseille, France*

[2]*Laboratoire Lagrange, UMR 7293, Université Nice Sophia-Antipolis, CNRS, Observatoire de la Côte d'Azur, F-06300 Nice, France*

[3]*Department of Physics and Astronomy and Pittsburgh Particle Physics, Astrophysics, and Cosmology Center (PITT PACC), University of Pittsburgh, Pittsburgh, PA 15260, USA*

ABSTRACT

We present 1D non-local thermodynamic equilibrium time-dependent radiative transfer simulations of a Chandrasekhar-mass delayed-detonation model which synthesizes 0.51 $M_\odot$ of ^{56}Ni, and confront our results to the Type Ia supernova (SN Ia) 2002bo over the first 100 d of its evolution. Assuming only homologous expansion, this same model reproduces the bolometric and multiband light curves, the secondary near-infrared (NIR) maxima, and the optical and NIR spectra. The chemical stratification of our model qualitatively agrees with previous inferences by Stehle et al., but reveals significant quantitative differences for both iron-group and intermediate-mass elements. We show that ± 0.1 $M_\odot$ (i.e. ± 20 per cent) variations in ^{56}Ni mass have a modest impact on the bolometric and colour evolution of our model. One notable exception is the *U* band, where a larger abundance of iron-group elements results in *less* opaque ejecta through ionization effects, our model with more ^{56}Ni displaying a higher near-ultraviolet flux level. In the NIR range, such variations in ^{56}Ni mass affect the timing of the secondary maxima but not their magnitude, in agreement with observational results. Moreover, the variation in the *I*, *J*, and K_s magnitudes is less than 0.1 mag within ∼10 d from bolometric maximum, confirming the potential of NIR photometry of SNe Ia for cosmology. Overall, the delayed-detonation mechanism in single Chandrasekhar-mass white dwarf progenitors seems well suited for SN 2002bo and similar SNe Ia displaying a broad Si II 6355 Å line. Whatever multidimensional processes are at play during the explosion leading to these events, they must conspire to produce an ejecta comparable to our spherically symmetric model.

Key words: radiative transfer – supernovae: general – supernovae: individual: SN 2002bo.

1 INTRODUCTION

The most widely accepted model for Type Ia supernovae (SNe Ia) is the thermonuclear disruption of a white dwarf (WD) star (Hoyle & Fowler 1960) in a binary system, although there is ongoing discussion about the combustion mode (pure deflagration or delayed detonation), the progenitor mass (Chandrasekhar mass or not), and the nature of the binary companion (another WD or a non-degenerate star). Observational evidence for diversity in the SN Ia population (e.g. van Kerkwijk, Chang & Justham 2010; Badenes & Maoz 2012) seems to require multiple progenitor channels or explosion mechanisms.

In a recent study, we found a promising agreement between a sequence of Chandrasekhar-mass delayed-detonation models and observations of SNe Ia at maximum light (Blondin et al. 2013, hereafter B13). The good match between our model DDC15 (∼0.5 $M_\odot$ of ^{56}Ni) and the standard SN 2002bo motivates an in-depth study of this model at earlier and later times.

SN 2002bo was first studied by Benetti et al. (2004), who favour a delayed-detonation explosion for this event based on the presence of intermediate-mass elements (IMEs) at high velocities and the lack of spectral signatures of C I/II associated with unburnt carbon at early times. Subsequent spectroscopic modelling by Stehle et al. (2005) revealed a chemical stratification qualitatively similar to the fast-deflagration W7 model of Nomoto, Thielemann & Yokoi (1984), but with an offset to higher velocities and strong mixing.

* E-mail: stephane.blondin@lam.fr

A striking feature of SN 2002bo is the large Doppler width of the Si II 6355 Å line around maximum light, which places this SN in the 'broad-line' subclass of Branch et al. (2006).[1] Such a broad Si II line is systematically predicted in maximum-light spectra of the delayed-detonation models presented in B13.

In the next section we briefly present the numerical set-up (hydrodynamics and radiative transfer). The observational data and our method of analysis are presented in Section 3. We then confront the predicted bolometric (Section 4), colour (Section 5), and spectroscopic (Section 6) evolution of our model to observations of SN 2002bo, both in the optical and near-infrared (NIR). We illustrate the sensitivity of our model results to ± 0.1 M$_\odot$ (i.e. ± 20 per cent) variations in ^{56}Ni mass in Section 7. We compare the abundance distributions of various elements in our input hydrodynamical model with those inferred by Stehle et al. (2005) in Section 8. A discussion on the nature of broad-lined SNe Ia and conclusions follow in Section 9.

2 NUMERICAL SET-UP

The hydrodynamics of the explosion and the radiative transfer treatment is analogous to that presented in B13 and Dessart et al. (2014c, hereafter D14c). We refer the reader to those papers for an in-depth discussion of our numerical set-up. As with all our previous SN studies, our models are iterated until convergence is achieved at all depths in the ejecta (see Appendix A).

We use the Chandrasekhar-mass delayed-detonation model DDC15 presented in B13, and summarize its basic properties in Table 1. Unlike B13, we apply a small radial mixing to the hydrodynamical input with a characteristic velocity width $\Delta v_{\rm mix} = 400$ km s^{-1} to smooth sharp variations in composition (see Dessart et al. 2014b, hereafter D14b). Moreover, we consider additional radioactive decay chains (only ^{56}Ni decay was considered in B13), resulting in non-negligible energy input beyond $\sim 15\,000$ km s^{-1} where the ejecta is deficient in ^{56}Ni (see model DDC10_A4D1 in D14b). More importantly, including the ^{48}Cr $\rightarrow$ ^{48}V $\rightarrow$ ^{48}Ti decay chain leads to a ~ 100-fold increase in the Ti mass fraction in the inner ejecta ($v \lesssim 13\,000$ km s^{-1}; see Fig. 1), which influences sizeably the opacity in the B band at maximum light and beyond.

The chemical stratification is typical of standard delayed-detonation models. Iron-group elements (IGEs; Sc to Ni, $M_{\rm tot} \approx 0.7$ M$_\odot$) dominate below $\sim 10\,000$ km s^{-1}. Despite the presence of ^{56}Ni at $\lesssim 2000$ km s^{-1} due to our imposed radial mixing, the innermost ejecta are dominated by *stable* IGEs. Intermediate-mass elements (Na to Ca, $M_{\rm tot} \approx 0.6$ M$_\odot$) are most abundant between $\sim 10\,000$ and $\sim 30\,000$ km s^{-1}. The outermost ~ 0.01 M$_\odot$ of the ejecta is dominated by the composition of the progenitor WD star (C/O, with traces of ^{22}Ne, and solar abundances for all other elements).
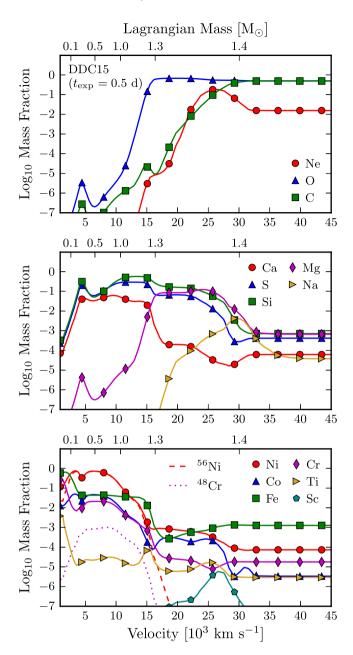
The ejecta density profile at the start of our radiative transfer calculations (0.5 d past explosion) is shown in Fig. 2. At these times, ultraviolet (UV) photons still interact with the ejecta material in shells moving at a velocity $> 40\,000$ km s^{-1}, so we linearly extrapolate the hydrodynamical input beyond $\sim 45\,000$ up to $\sim 70\,000$ km s^{-1}, as

[1] Given the associated large blueshift at maximum absorption ($> 12\,000$ km s^{-1} at maximum light), this SN is also part of the 'high-velocity' subclass of Wang et al. (2009) and the 'high-velocity-gradient' subclass of Benetti et al. (2005).

Table 1. Model parameters and nucleosynthetic yields for selected species at the start of our radiative transfer calculations (0.5 d past explosion). The ^{56}Ni mass is given at $t_{\rm exp} \approx 0$. Models DDC10 and DDC17 will be discussed in Section 7.

Model	$\rho_{\rm tr}$ (g cm^{-3})	$E_{\rm kin}$ (erg s^{-1})	$v(^{56}{\rm Ni})$ (km s^{-1})	$^{56}{\rm Ni}_{t=0}$ (M$_\odot$)	Ni (M$_\odot$)	Co (M$_\odot$)	Fe (M$_\odot$)	Ti (M$_\odot$)	Sc (M$_\odot$)	Ca (M$_\odot$)	S (M$_\odot$)	Si (M$_\odot$)	Mg (M$_\odot$)	Na (M$_\odot$)	O (M$_\odot$)	C (M$_\odot$)
DDC15	1.8(7)	1.465(51)	1.12(4)	0.511	0.516	3.44(−2)	0.114	1.11(−4)	4.09(−8)	4.53(−2)	0.197	0.306	1.14(−2)	1.68(−5)	0.105	2.73(−3)
DDC10	2.3(7)	1.520(51)	1.16(4)	0.623	0.622	4.11(−2)	0.115	1.10(−4)	2.90(−8)	4.10(−2)	0.166	0.257	9.95(−3)	1.25(−5)	0.101	2.16(−3)
DDC17	1.6(7)	1.459(51)	1.08(4)	0.412	0.421	2.84(−2)	0.112	1.14(−4)	6.16(−8)	4.73(−2)	0.222	0.353	1.79(−2)	2.47(−5)	0.152	3.80(−3)

Notes. Numbers in parenthesis correspond to powers of 10. The deflagration velocity is set to 3 per cent of the local sound speed ahead of the flame for all models; $\rho_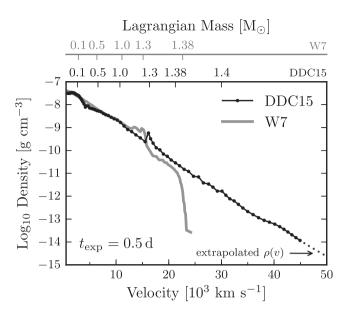{\rm tr}$ is the transition density at which the deflagration is artificially turned into a detonation; $E_{\rm kin}$ is the asymptotic kinetic energy; and $v(^{56}{\rm Ni})$ is the velocity of the ejecta shell that bounds 99 per cent of the total ^{56}Ni mass.

Figure 1. Abundance profiles in velocity space for C/O/Ne (top), selected IMEs (middle), and IGEs (bottom; the profiles for ^{56}Ni and ^{48}Cr at this time are shown as a dashed and dotted line, respectively) in model DDC15 at the start of our radiative transfer simulations (0.5 d past explosion). The upper abscissa shows the Lagrangian mass coordinate.

Figure 2. Density profile at the start of our radiative transfer simulations (0.5 d past explosion; black line), compared to the W7 model (grey line) of Nomoto et al. (1984). The solid dots correspond to the initial radial grid used in CMFGEN. The dotted curve shows the extrapolated density profile beyond ∼45 000 km s^{-1} (see text). The upper axis gives the Lagrangian mass coordinate for both DDC15 (black) and W7 (grey).

The radial mixing applied to the hydrodynamical input and the extended radial grid result in small differences in abundance between the DDC15 model presented in B13 and the version used in this paper. In particular, the initial ^{56}Ni mass for this model is now ∼0.51 M$_\odot$, cf. ∼0.56 M$_\odot$ in B13 (see their table 1). These differences only have a modest impact at bolometric maximum: a bolometric rise time of 17.57 d (cf. 17.76 d in B13), a peak bolometric luminosity of 1.14×10^{43} erg s^{-1} (cf. 1.22×10^{43} erg s^{-1}), and a $B - R$ colour of 0.04 mag (cf. −0.02 mag).
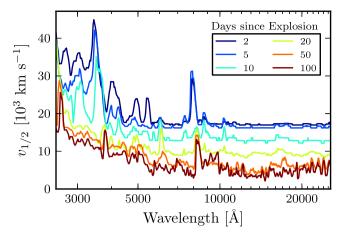
In what follows, we use model DDC15 to discuss SN 2002bo and broad-lined SNe Ia in general. However, we also study the sensitivity of our results by comparing the predicted light curves and spectra of delayed-detonation models endowed initially with ±20 per cent of mass of ^{56}Ni (models DDC10 and DDC17 in Table 1). This comparison is particularly instructive to understand the degeneracy (or lack thereof) of SN Ia properties.

3 OBSERVATIONAL DATA AND METHODOLOGY

Our data on SN 2002bo are mostly taken from Benetti et al. (2004), with additional optical spectra from Blondin et al. (2012) and Silverman et al. (2012). We use the near-infrared (JHK_s) photometry published by Krisciunas et al. (2004a). We select spectra whose relative flux calibration agrees with photometry-based colours to within 0.1 mag. As in B13, we adopt a recession velocity $cz = 1293$ km s^{-1} for the host galaxy, a distance modulus $\mu = 31.90 \pm 0.20$ mag, and a total reddening $E(B - V) = 0.41 \pm 0.07$ mag.

The method for generating pseudo-bolometric light curves for both models and data is analogous to that presented in B13. We specify each time the bluest and the reddest band used in the integration, such that $L_{U \to K_s}$ corresponds to the luminosity (in erg s^{-1}) obtained by integrating $UBVRIJHK_s$ magnitudes.

Since there is no good definition of a photosphere through opacity means in SNe Ia, we characterize the spectrum-formation region

done in D14b (dotted line in Fig. 2). The density profile is reminiscent of standard delayed-detonation models (see e.g. Khokhlov, Müller & Höflich 1993), with a quasi-exponential decrease with velocity. Also shown is the density profile of the W7 model used as a reference in many SN Ia studies. It is nearly indistinguishable from our model below ∼10 000 km s^{-1} (or within a Lagrangian mass coordinate of ∼1 M$_\odot$). The key difference lies in the amount of mass contained at high velocities: it is a factor of ∼2 larger beyond ∼15 000 km s^{-1} in DDC15, resulting in a ∼20 per cent larger kinetic energy (∼1.5×10^{51} erg cf. ∼1.2×10^{51} erg for W7; see Table 1). The composition is also drastically different, with IMEs confined to ≲15 000 km s^{-1}, while they are abundant beyond 20 000 km s^{-1} in DDC15.

Figure 3. Illustration of the wavelength dependence of the spectrum-formation region, represented here using the velocity above which 50 per cent of the flux at a given wavelength is emitted. This velocity is computed based on equation (3), but replacing the wavelength-averaged flux contribution $\overline{\delta F(v)}$ of equation (2) with the non-averaged $\delta F(r, \lambda, t)$ of equation (1).

using the spatial distribution of the optical (3000–10 000 Å) flux instead. The fractional contribution to the total flux at wavelength λ from a given ejecta shell at radius r and thickness dr at time t since explosion is

$$\delta F(r, \lambda, t) = \frac{2\pi}{D^2} \int \Delta z\, \eta(p, z, \lambda, t)\, e^{-\tau(p, z, \lambda, t)}\, p\, dp, \qquad (1)$$

where D is the physical distance, Δz is the projected shell thickness for a ray with impact parameter p, η is the emissivity along the ray at p and z, and τ is the ray optical depth (at λ) at the ejecta location (p, z). Because of homologous expansion ($v = r/t$), surfaces of constant projected velocity are planes perpendicular to the z direction. Hence, the quantity $\delta F(r, \lambda, t)$ mixes contributions from regions with the same radial velocity but with very different projected velocities, hence Doppler shift. The averaged contribution of a shell with velocity v (corresponding to $r + dr/2$) over the wavelength interval $[\lambda_1, \lambda_2]$ is given by

$$\overline{\delta F(v)} = \frac{\int_{\lambda_1}^{\lambda_2} \delta F(r, \lambda, t)\, d\lambda}{|\lambda_1 - \lambda_2|}. \qquad (2)$$

A representative velocity for the spectrum-formation region in the wavelength range λ_1 to λ_2 may be the velocity above which 50 per cent of the flux in that range is emitted, noted $v_{1/2}$, such that

$$\frac{\sum_{v \geq v_{1/2}} \overline{\delta F(v)}}{\sum_{\text{all } v} \overline{\delta F(v)}} = \frac{1}{2}, \qquad (3)$$

where the sum in the denominator runs over the entire velocity grid spanned by our simulation.

In what follows this velocity is only used for illustration purposes, as the averaging in equation (2) occults the strong variation of $v_{1/2}$ with wavelength (Fig. 3). This variation reflects the dominance of line opacity in SN Ia ejecta (see e.g. Pinto & Eastman 2000).

4 BOLOMETRIC EVOLUTION

The pseudo-bolometric light curves for both our DDC15 model and SN 2002bo are shown in Fig. 4. Our model predicts a rise to bolometric maximum of ∼17.6 d, while the first observations of SN 2002bo are ∼14 d before peak. At these early times, the

bolometric evolution is well matched by our model, albeit with a slightly larger luminosity (but still within the errors). This suggests the ^{56}Ni distribution is adequate, in particular its presence at $\gtrsim 15\,000$ km s^{-1}. In W7, the ^{56}Ni mass fraction drops to 10^{-5} at ∼12 000 km s^{-1}, and the early-time luminosity is significantly lower than observed in SN 2002bo (see also Stehle et al. 2005).

A power-law fit $L(t) \propto t^\alpha$ to the early ($t_{\text{exp}} \lesssim 3$ d) bolometric light curve of model DDC15 yields $\alpha = 3.4$ (Table 2). Deviations from a 'fireball' model (for which $\alpha = 2$; Nugent et al. 2011) are expected theoretically and confirmed observationally, as in the recent SN 2013dy (Zheng et al. 2013). Variations in the early-time luminosity can result from outward mixing of ^{56}Ni (e.g. Piro & Nakar 2014), or from structural changes in the outer ejecta, as in the pulsational-delayed-detonation models of D14b.

The lower panel of Fig. 4 gives the fractional contribution to the total bolometric luminosity of various filter sets, as well as in the UV (<3000 Å) and IR (>1 μm) ranges. At maximum light, we recover 94 per cent of the true bolometric luminosity with our $U \rightarrow K_s$ pseudo-bolometric light curve (see also Table B1). The remaining 6 per cent is mostly emitted blueward of the U band.

From bolometric maximum until the onset of the radioactive tail ∼35 d later the γ-ray escape fraction increases from ∼5 to ∼50 per cent. The decline in bolometric magnitude between maximum light and 15 d later (noted ΔM_{15} in Table 2) is 0.72 mag, comparable to that inferred for SN 2002bo based on its $U \rightarrow K_s$ pseudo-bolometric light curve (∼0.85 mag).

Past maximum, the transition to an optically thin ejecta is concomitant with a shift in ionization and a greater release of radiation energy, causing a small bump in the bolometric light curve around ∼20 d past maximum light (∼30 d past maximum in SN 2002bo; see Fig. 4).

Past ∼30 d from maximum light (∼50 d since explosion), the bolometric luminosity follows the instantaneous rate of energy deposition. The γ-ray escape fraction continues to increase, reaching ∼80 per cent at ∼100 d past explosion. The late-time (>50 d past maximum) pseudo-bolometric ($U \rightarrow I$) decline is compatible with SN 2002bo (∼0.024 mag d^{-1} cf. ∼0.022 ± 0.007 mag d^{-1}).

The kinetic energy, ^{56}Ni mass, and ejecta mass of our model yield a bolometric light curve consistent with observations of SN 2002bo at all times. This represents a compelling check for the standard Chandrasekhar-mass delayed-detonation model for this class of SN Ia light-curve morphology. Moreover, the good match with a 1D model suggests that asymmetries, if present, may only have a minor role in shaping the bolometric light curve of SN 2002bo.

5 PHOTOMETRIC EVOLUTION

The colour evolution of SNe Ia reflects both the global evolution of ejecta properties (temperature, mean ionization) and the wavelength-dependent opacity, and is thus very difficult to accurately model.

Initially, all bands experience a steep brightening due to the increase in radius. The brightening is steeper for the bluer bands (see the α exponent in Table 3) due to the temperature increase in the spectrum-formation layers (solid dots in Fig. 5), which shifts the optical and NIR colours shown in Fig. 6 to the blue. Because of the lower opacity/emissivity compared to the optical, the NIR flux starts to *decrease* as the spectral energy distribution (SED) hardens, as early as 7 d prior to bolometric maximum for the H and K_s bands in model DDC15 (Fig. 7). In SN 2002bo, the initial peak in these bands occurs ∼3 d later than in our models, similar to the evolution in the J band (which is well matched by our model).
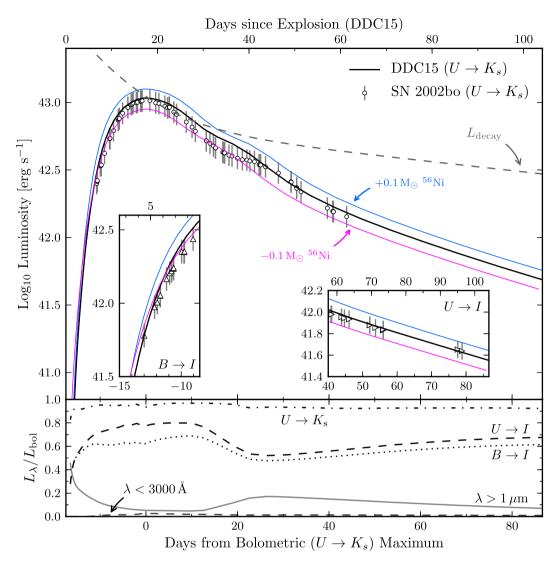
Figure 4. Top: pseudo-bolometric ($U \to K_s$) light curve for model DDC15 (black) and SN 2002bo (open circles). The error bars take into account measurement, extinction, and distance errors. The grey dashed line shows the instantaneous rate of decay energy. Coloured lines correspond to models with $\pm 0.1\,M_\odot$ of ^{56}Ni compared to DDC15. We show close-up views of the early-time $B \to I$ (left-hand inset) and late-time $U \to I$ (right-hand inset) pseudo-bolometric light curves, due to the lack of U band or NIR data at these times. The upper abscissa gives the time since explosion for model DDC15. Bottom: contribution of the $U \to K_s$ (dash–dotted line), $U \to I$ (dashed line), and $B \to I$ (dotted line) pseudo-bolometric luminosities to the total bolometric luminosity. Also shown are the contributions of the UV ($\lambda < 3000$ Å; grey solid line) and IR ($\lambda > 1$ μm; grey dashed line) ranges.

Table 2. Bolometric properties. Models DDC10 and DDC17 will be discussed in Section 7.

Model	^{56}Ni ($M_\odot$)	$t_{\rm rise}$ (d)	α	$L_{\rm peak}$ (erg s^{-1})	ΔM_{15} (mag)	Q_γ	$\mathcal{F}_{\rm dep}$
DDC15	0.511	17.57	3.4	1.14(43)	0.72	1.04	0.95
DDC10	0.623	17.13	3.3	1.38(43)	0.74	1.00	0.95
DDC17	0.412	18.60	3.3	9.10(42)	0.67	0.99	0.97

Notes. Numbers in parenthesis correspond to powers of 10; α is the exponent of the power-law fit to the early-time ($t_{\rm exp} \lesssim 3$ d) luminosity, $L(t) \propto t^\alpha$; ΔM_{15} is the bolometric magnitude decline between bolometric maximum and 15 d after; Q_γ is the ratio of the peak bolometric luminosity ($L_{\rm peak}$) to the instantaneous decay luminosity; and $\mathcal{F}_{\rm dep}$ is the fraction of decay energy at peak actually deposited in the ejecta.

In the optical, the shorter rise times in the U and B bands with respect to V and R reflects the temperature decline in the spectrum-formation region after about 1 week past explosion. By maximum light, most of the flux originates from layers $\lesssim 15\,000$ km s^{-1} where the temperature is decreasing (Fig. 5).

The $U - V$ and $B - V$ colours shift to the red at ~ 10 d past explosion (1 week before B-band maximum), i.e. 10–20 d before the other colours shown in Fig. 6. This earlier shift in colour results from the increase in opacity from once-ionized IGEs that deplete the flux in U and B relative to redder bands.

The $\Delta m_{15}(B)$ parameter for our model is 1.03 mag, consistent with that inferred for SN 2002bo (1.18 $\pm$ 0.07 mag; see Table 3). In the redder optical bands and in the NIR range, the post-maximum decline rate is sensitive to the location of line emission. In the IHK_s bands, line emission is sufficient to maintain a near-constant flux level despite the overall decline in bolometric luminosity

Table 3. Light-curve properties. For each parameter, the upper line corresponds to model DDC15 (the upper and lower values, when added to the DDC15 value, correspond to models DDC10 and DDC17, respectively), and the lower line to SN 2002bo (1σ errors are given in between parentheses).

Parameter	U	B	V	R	I	J	H	K_s
α in $L(t) \propto t^\alpha$	$4.0^{+1.2}_{+1.4}$	$5.9^{-0.1}_{-0.3}$	$5.3^{-0.6}_{-0.4}$	$4.1^{-0.6}_{-0.3}$	$3.7^{-0.5}_{-0.2}$	$2.6^{-0.1}_{-0.1}$	$2.6^{-0.1}_{-0.1}$	$2.5^{-0.0}_{-0.0}$
($t_{exp} < 3$ d)	...	...	...	...	...	...	...	...
Δt_{peak}	$-1.10^{-0.65}_{+0.57}$	$-0.39^{+0.57}_{-0.65}$	$+3.25^{-0.24}_{-0.07}$	$+2.19^{+0.39}_{-0.99}$	$+1.55^{-0.53}_{-0.29}$	$-4.05^{-1.23}_{+0.69}$	$-6.55^{-1.19}_{+1.30}$	$-6.62^{-0.89}_{+0.68}$
(d)	$-0.68 (0.70)$	$+0.61 (0.60)$	$+2.44 (0.67)$	$+2.15 (0.54)$	$-1.47 (0.34)$	$-1.39 (0.14)$	$-1.10 (0.14)$	$-0.84 (0.28)$
$\Delta t_{2nd\ max}$	...	...	...	...	$+20.42^{+2.91}_{-3.50}$	$+23.42^{+1.99}_{-2.08}$	$+20.66^{+2.91}_{-3.63}$	$+20.84^{+2.35}_{-3.51}$
(d)	...	...	...	...	$+24.45 (1.52)$	$+28.36 (0.39)$	$+24.93 (0.42)$	$+24.81 (0.98)$
M_{peak}	$-19.40^{-0.34}_{+0.59}$	$-19.15^{-0.19}_{+0.22}$	$-19.23^{-0.17}_{+0.17}$	$-19.20^{-0.13}_{+0.13}$	$-18.83^{-0.04}_{+0.03}$	$-18.53^{+0.02}_{-0.03}$	$-18.13^{+0.02}_{-0.07}$	$-18.07^{+0.00}_{-0.04}$
(mag)	$-19.38 (0.22)$	$-19.20 (0.11)$	$-19.20 (0.10)$	$-19.10 (0.09)$	$-18.75 (0.10)$	$-18.43 (0.14)$	$-18.18 (0.14)$	$-18.13 (0.14)$
$M_{2nd\ max}$	...	...	...	...	$-18.86^{+0.07}_{-0.00}$	$-17.93^{+0.14}_{-0.02}$	$-18.83^{+0.06}_{+0.01}$	$-18.73^{+0.06}_{+0.01}$
(mag)	...	...	...	...	$-18.33 (0.13)$	$-17.44 (0.13)$	$-18.21 (0.14)$	$-18.05 (0.15)$
ΔM_{15}	$1.30^{-0.17}_{+0.10}$	$1.03^{-0.10}_{+0.24}$	$0.71^{-0.05}_{+0.17}$	$0.54^{+0.08}_{-0.03}$	$0.08^{+0.24}_{-0.12}$	$1.31^{-0.12}_{-0.11}$	$0.06^{+0.07}_{-0.19}$	$-0.04^{-0.02}_{-0.06}$
(mag)	$1.53 (0.13)$	$1.18 (0.07)$	$0.70 (0.03)$	$0.71 (0.04)$	$0.64 (0.03)$	$1.65 (0.06)$	$0.37 (0.03)$	$0.42 (0.07)$
$\Delta M/\Delta t_{50+}$	$0.024^{+0.001}_{+0.000}$	$0.016^{+0.001}_{+0.000}$	$0.026^{+0.001}_{-0.001}$	$0.030^{+0.001}_{-0.001}$	$0.034^{+0.002}_{-0.002}$	$0.056^{+0.001}_{-0.002}$	$0.041^{-0.000}_{+0.000}$	$0.037^{-0.002}_{+0.002}$
(mag d^{-1})	$0.019 (0.013)$	$0.011 (0.005)$	$0.023 (0.003)$	$0.033 (0.002)$	$0.041 (0.001)$	...	...	...

Notes. The I-band light curves for models DDC10 and DDC15 have several glitches around maximum light, hence the parameter values are less reliable; Δt_{peak} is the time difference between maximum light in a given band (*first* maximum for $IJHK_s$) and pseudo-bolometric ($U \to K_s$) maximum; $\Delta t_{2nd\ max}$ is the time difference between the secondary maximum ($IJHK$ only) and pseudo-bolometric ($U \to K_s$) maximum; and $\Delta M/\Delta t_{50+}$ is the average magnitude decline rate past $+50$ d from maximum light.

Figure 5. Evolution of the gas temperature profile (top) and of the cobalt ionization fraction (bottom) in model DDC15, between 1 and 100 d since explosion (note the logarithmic time steps). Solid dots mark the velocity location above which 50 per cent of the optical flux is emitted, which we use to characterize the spectrum-formation region (see Section 3).

($\Delta M_{15}(IHK_s) \approx 0$ mag), while the weaker line emission within the J band causes a more pronounced decline ($\Delta M_{15}(J) \approx 1.3$ mag).

At late times, the colours shown in Fig. 6 become progressively bluer despite the near-constant temperature (7000–8000 K in the ejecta layers between 5000 and 15 000 km s^{-1}; see Fig. 5): the low ejecta densities favour the formation of forbidden lines, whose wavelength location impacts the colour evolution independent of temperature.
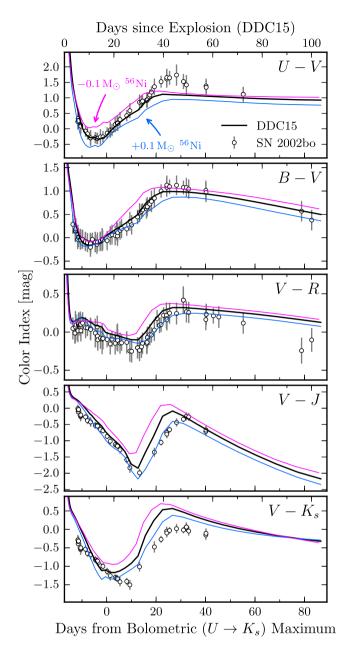
Our model reproduces the complex evolution of the optical and NIR colours of SN 2002bo out to ∼80 d past maximum light. This gives us confidence that the apparent red colours of SN 2002bo are indeed due to extinction in the host galaxy. Moreover, the observed colour curves are corrected for reddening using the classical Cardelli, Clayton & Mathis (1989) extinction law with a standard value of the total-to-selective extinction ratio $R_V = 3.1$.

However, the model is very red within the first ∼5 d since explosion, where we lack SN 2002bo data. Earlier observations of several other SNe Ia (e.g. SN 2011fe, Nugent et al. 2011; SN 2013dy, Zheng et al. 2013), all of which display a narrower Si II 6355 Å line than SN 2002bo around maximum, reveal significantly bluer colours than predicted by our model. Such blue colours at early times are difficult to reproduce with standard 1D delayed-detonation models, even with strong outward mixing of ^{56}Ni, and instead appear to require some form of hydrodynamical interaction to heat up the outer ejecta layers, as in the pulsating delayed-detonation models of D14b.[2] Earlier observations of a broad-lined SN Ia such as SN 2002bo would enable to check the prediction of red early-time optical colours in our model.

6 SPECTROSCOPIC EVOLUTION

We describe below the evolution of the optical (Fig. 8) and NIR (Fig. 9) spectra of our model and compare them to SN 2002bo

---

[2] Although such an interaction serves to decelerate these outer ejecta layers, inhibiting the formation of broad spectral lines as in SN 2002bo.

Figure 6. Comparison of colour curves for model DDC15 (black) and SN 2002bo (dereddened; open circles). The error bars take into account measurement and extinction errors. Coloured lines correspond to models with $\pm 0.1\,M_\odot$ of ^{56}Ni compared to DDC15. Note that the redder colour curve corresponds to the model with *less* ^{56}Ni (DDC17). The upper abscissa gives the time since explosion for model DDC15.

observations. Tables with detailed line identifications and a collection of plots illustrating the influence of individual ions on the synthetic spectra are available in Appendices C and D, respectively.

6.1 Early evolution

During the first $\sim$10 d past explosion, the majority of the optical flux emerges from the IME-rich regions of the ejecta at $\gtrsim$15 000 km s^{-1}. The optical spectrum is thus dominated by broad lines of Mg II, Si II, S II, and Ca II. We also note the presence of O I 7773 Å, which causes a deep absorption blueward of the Ca II 8500 Å triplet. Iron-group

elements, most notably Sc II, Ti II, Cr II, Fe II, Co II, and Ni II, also contribute to the flux shortward of $\sim$5000 Å.

We obtain high-velocity absorption ($>$25 000 km s^{-1} blueshifts) in both the Ca II H&K and 8500 Å triplet features. These remain optically thick well beyond 30 000 km s^{-1} where the Ca abundance is at its primordial solar value ($X \approx 6 \times 10^{-5}$), but their blue wings are affected by absorption from other lines and thus cannot easily serve as probes of the progenitor metallicity (see also Lentz et al. 2000 in the context of the W7 model). The Si II 3858 Å line has negligible impact on our synthetic spectra, and the predicted double-absorption feature at $\sim$3500 Å seen, e.g. in the $-$7.7 d spectrum results from Ca II alone. Multiple absorption components in both Ca II features are routinely observed in early-time SN Ia spectra (e.g. Childress et al. 2014).

Unburnt material is located in the outermost ($\gtrsim$20 000 km s^{-1}) low-density layers of the ejecta. This configuration makes the associated spectral signatures of carbon (e.g. C II 6578 Å) too weak to be visible. The O I 7773 Å line can in principle serve to constrain the amount of unburnt oxygen, but it forms below $\sim$25 000 km s^{-1} in our model and hence results in part from C-burning ash.

In the NIR range, our model reproduces the overall shape of the earliest spectrum of SN 2002bo at $-$8.5 d ($\sim$9 d past explosion based on model DDC15), but predicts a higher flux level than observed ($F_{\rm scl} = 0.64$). Three ions are responsible for the spectral signatures seen: O I, Mg II, and Si II (see Fig. C2, upper right-hand panel). The two most notable features at these early times are a P-Cygni profile due to the Mg II 10927 Å triplet and a broad emission feature at $\sim$1.7 μm due to the Si II 16931 Å doublet.

Lines from IGEs are completely absent from the NIR range at these early times, although lines of Sc II, Ti II, Cr II, and Fe II–III (with weaker absorptions from Co II and Ni II in the U band) contribute to the optical flux. The majority of the NIR flux emerges from ejecta layers $\lesssim$20 000 km s^{-1} where most IGEs are at least twice ionized, and contribute opacity at much shorter wavelengths.

The earliest spectrum at $\sim$13 d before bolometric maximum, however, shows that we predict too little flux around 4000 Å, due to excess absorption from Sc II 4247 Å and several Ti II lines, and that the blue extent of certain features is not well matched, in particular the Fe II absorption complex around 4800 Å, and the two Si II 5972 and 6355 Å features. The O I 7773 Å absorption is also too strong in our model. These discrepancies are related to the low ejecta ionization fraction at $\sim$20 000 km s^{-1} (Fig. 5), and suggest a stronger outward mixing of ^{56}Ni than adopted here. Another possibility is that our extrapolated density profile at large velocity is steeper in reality (see Fig. 2).

6.2 Maximum-light phase

Around maximum light the optical spectra are still dominated by strong lines of singly ionized IMEs, with IGEs absorbing the flux at $\lesssim$5000 Å. The drop in the Mg and O mass fractions below $\sim$15 000 km s^{-1} results in a gradual weakening of the Mg II and O I 7773 Å lines and reveals the transition from the C-burning to the O-burning regime. We note the disappearance of the high-velocity absorption associated with Ca II H&K and the 8500 Å triplet, as these transitions turn thin beyond $\sim$20 000 km s^{-1}.

In the NIR, we note the appearance of emission features associated with IGEs, most notably permitted Co II and forbidden Co III transitions. There are no published NIR spectra of SN 2002bo around maximum light to compare against our model.
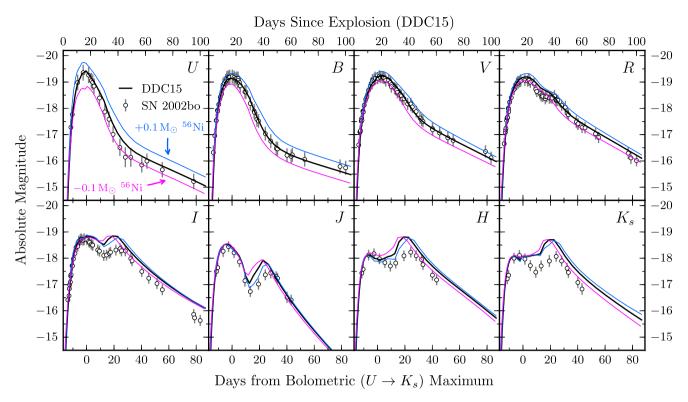
Figure 7. Optical (*UBVRI*) and NIR (*JHK*$_s$) light curves for model DDC15 (solid lines) compared to SN 2002bo (dereddened; open circles). The error bars take into account measurement, extinction, and distance errors. Coloured lines correspond to models with ±0.1 M$_\odot$ of ^{56}Ni compared to DDC15. The upper abscissa gives the time since explosion for model DDC15.

6.3 Post-maximum and transition to nebular phase

From ∼10 until ≲40 d past maximum light the majority of the flux emerges from the outer IGE-rich regions of the ejecta (≲10 000 km s^{-1}). Some strong lines of IMEs survive in the optical range (Si II, S II, Ca II), although they become weaker and narrower with time. Most of the spectrum is now shaped by lines of IGEs such as Ti II, Cr II, Fe II–III, and Co II–III.

The SED becomes redder due to the gradual drop in temperature in the inner ejecta layers. Radiation cooling dominates over expansion cooling, with a growing importance played by forbidden-line transitions. A notable example is the 5900 Å feature, well matched by our model, and associated with [Co III] 5888 Å. This feature is often mistaken for Na I D (see discussion in Dessart et al. 2014a).

This cooling further enhances absorption by Cr II/Ti II transitions around 4000–4300 Å. Several Cr II lines are responsible for the rapid change in relative flux around ∼5300 Å between +16.2 and +28.2 d (Fig. 8), which reflects the rapid evolution of the Cr II/III ratio.

In the NIR, III→II recombination of IGEs causes a gradual weakening of Co III lines (primarily forbidden transitions) and a strengthening of Co II lines (primarily permitted). In some bands (*H* and *K*$_s$), emission by Co II is sufficient to maintain a near-constant flux level and causes an earlier shift to the red of the *V* − *K*$_s$ colour curve with respect to *V* − *J* (Fig. 6).

The strengthening of the Co II emission is partly responsible for the mismatch in the Ca II 8500 Å triplet emission profile between our model and SN 2002bo. Co II lines blueward of ∼8500 Å emit photons in the inner ejecta (≲10 000 km s^{-1}) that are redshifted into resonance with the Ca II 8500 Å triplet transitions in higher velocity shells (see also D14c). The resulting boost in emissivity explains the

slower decline in the *I* band in our model compared to SN 2002bo (cf. Fig. 7 and Table 3).

6.4 Late-time evolution out to ∼100 d past explosion

From ∼40 d past maximum onwards the spectrum-formation region is almost exclusively located in the IGE-rich layers of the ejecta below 10 000 km s^{-1}. Apart from the two strong Ca II H&K and 8500 Å triplet features and traces of Si II 6355 Å, which retain their P-Cygni profile morphology, the only optical lines from IMEs are optically thin transitions of [S II], [S III], and [Ar III]. Beyond 1 µm, the only emission from IMEs comes from [S II] and Ca II transitions, although the impact on the observed flux is negligible given the overlap with stronger emission from Fe II and Co II.

Non-thermal ionization prevents a complete III→II recombination of IGEs in the inner ejecta, resulting in increasing emission from lines of [Fe III] and [Co III], now favoured due to the low ejecta density. Some of these lines represent a fair fraction of the total flux in a given band: At ∼100 d past explosion, the [Fe III] 4658 Å and [Co III] 5888 Å lines alone contribute ∼15 per cent of the total flux in the *B* and *R* bands, respectively. The ratio of the total flux emitted in both lines follows the increase in the Fe/Co abundance ratio resulting from ^{56}Co → ^{56}Fe decay (see also Kuchner et al. 1994). The late-time colour evolution is thus largely determined by the wavelength location of individual strong transitions and no longer reflects the evolution of the ejecta temperature, which remains almost constant in the spectrum-formation region at these times (Fig. 5).

In the NIR, we predict the gradual emergence of [Ni II] 1.94 µm, due to *stable* Ni in the innermost ejecta (≲2000 km s^{-1}; see Fig. 1), resulting from burning at high densities characteristic of a

Figure 8. Optical spectroscopic evolution of model DDC15 (red) compared to SN 2002bo (black), between -12.9 and $+83.6$ d from pseudo-bolometric ($U \rightarrow K_s$) maximum. The tick marks on the ordinate give the zero-flux level. The observed spectra have been deredshifted, dereddened, and scaled to match the absolute V-band magnitude inferred from the corresponding photometry. An additional scaling (F_{scl}; green label) has been applied to the synthetic spectra to reproduce the mean observed flux in the range 5000–6500 Å.
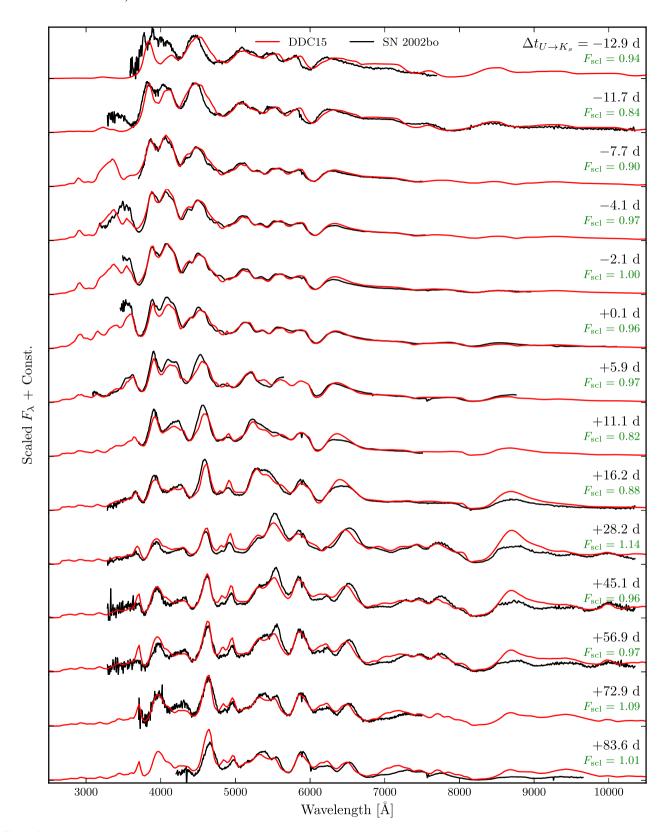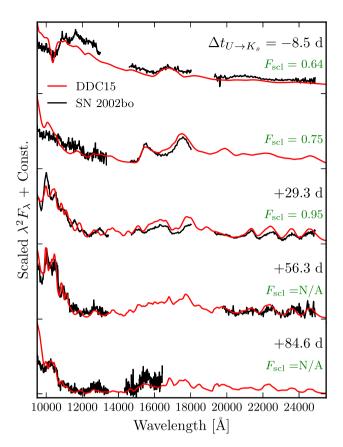
Figure 9. NIR spectroscopic evolution of model DDC15 (red) compared to SN 2002bo (black), between -8.5 and $+84.6$ d from pseudo-bolometric ($U \rightarrow K_s$) maximum. The flux has been scaled by λ^2 for better visibility, and the tick marks on the ordinate give the zero-flux level. The observed spectra have been deredshifted, dereddened, and scaled to match the absolute J-band magnitude inferred from the corresponding photometry, when available. An additional scaling (F_{scl}; green label) has been applied to the synthetic spectra to reproduce the mean observed flux in the range 10 000–11 500 Å.

Chandrasekhar-mass WD progenitor (see e.g. Höflich et al. 2002). However, most of the emission just blueward of 2 μm is in fact due to lines of [Co III] in our model, not [Ni II] as recently suggested by Friesen et al. (2014) for SNe 2001fe, 2003du, and 2014J based on the 1D delayed-detonation models of Domínguez, Höflich & Straniero (2001). Unfortunately, the NIR spectrum of SN 2002bo at $+56.3$ d does not cover this feature.

The match between the spectra of model DDC15 and SN 2002bo over the first ~100 d of its evolution suggests the composition of the ejecta in our model is adequate at all depths. It also shows our time-dependent radiative transfer treatment consistently predicts the evolution of the gas properties, in particular its ionization state.

7 SENSITIVITY TO ^{56}Ni MASS

Our model DDC15 seems well suited to match the observed properties of SN 2002bo. In this section, we investigate whether delayed-detonation models with ± 0.1 M$_\odot$ (i.e. ± 20 per cent) variations in ^{56}Ni mass also provide a satisfactory match to this event (models DDC10 and DDC17 of B13; see Table 1). This is of particular relevance to assess the actual accuracy of abundance determinations in SNe Ia and to understand the degeneracy (or lack thereof) of their properties. We discuss in turn the impact on the early brightening phase (Section 7.1), on the post-maximum decline rate and the

width–luminosity relation (Section 7.2), on the late-time evolution (Section 7.3), and on the relative homogeneity of SN Ia properties in the NIR (Section 7.4). Finally, we comment on the impact of the IGE abundance on the near-UV flux level (Section 7.5).

7.1 Early brightening phase and high-velocity features

The early rate of increase in bolometric luminosity is largely insensitive to the ^{56}Ni mass, as seen through the <3 per cent variation in the power-law exponent α in Table 3. The same is true in individual bands, although it is larger in *UBVR* and is hardly noticeable in *I* and the NIR bands (Fig. 7). This suggests that the early-time luminosity, if powered by ^{56}Ni alone, is more sensitive to mixing than slight variations in total ^{56}Ni mass (see D14b). Indeed, mixing can increase the ^{56}Ni mass fraction by several orders of magnitude in the outermost layers (see also Section 8) where an increase in ^{56}Ni mass only results in a modest variation of the outer extent of the ^{56}Ni distribution (cf. $v(^{56}$Ni) column in Table 1).

Spectroscopically, the effect is most clearly seen in the UV range (blueward of ~3500 Å; see Fig. 10), through variations in the absorption by once-ionized IGEs (Sc II, Ti II, Cr II, Fe II, Co II, and Ni II). The relative strength of the high-velocity components to the Ca II H&K and 8500 Å triplet absorptions also varies significantly amongst our three models. They are weaker in our model with more ^{56}Ni (DDC10) due to the higher Ca ionization at 25 000–35 000 km s^{-1}. Conversely, the higher excitation in the outer ejecta leads to enhanced absorption in the blue wings of several lines, including the Fe II absorption complex around 4800 Å. The increase in ^{56}Ni mass is not sufficient to match the large Si II 6355 Å blueshift at early times, which might indicate a greater outward mixing of ^{56}Ni (D14b; see also Baron et al. 2012).

7.2 Post-maximum decline and the width–luminosity relation

The bolometric post-maximum decline rate (parametrized via the ΔM_{15} parameter in Table 2) changes by less than 0.1 mag from model DDC10 to DDC17. Part of this degeneracy with ^{56}Ni mass stems from the increase in the γ-ray escape fraction for models with more ^{56}Ni. By 20 d past explosion, ~10 per cent of the decay energy directly leaks out of the ejecta in model DDC10, cf. only ~5 per cent in DDC17.

However, an increase in the ^{56}Ni mass results in bluer colours at any given time and a more gradual shift to redder colours (Fig. 6), which affects the post-maximum decline rate in the individual bands. In the *B* band, the ΔM_{15} parameter varies by ~0.4 mag (0.92, 1.03, and 1.27 mag in order of decreasing ^{56}Ni mass), or four times the bolometric variation. Despite the relatively narrow range in peak M_B, we can compute a width–luminosity relation for these three models: $M_B = 1.12[\Delta m_{15}(B) - 1.1] - 19.11$. This width–luminosity relation is consistent with the observed one for broad-lined SNe Ia in Blondin et al. (2012).

Spectroscopically, the most notable impact of ^{56}Ni mass (other than the absolute flux difference) is in the Cr II-dominated region around 5300 Å. As noted in Section 6.3, this region is particularly sensitive to the Cr ionization level.

7.3 Late-time evolution

The late-time bolometric magnitude decline is the same for our three models (~0.028 mag d^{-1}), i.e. the rate of change of the γ-ray escape fraction is nearly identical. This is a natural consequence of
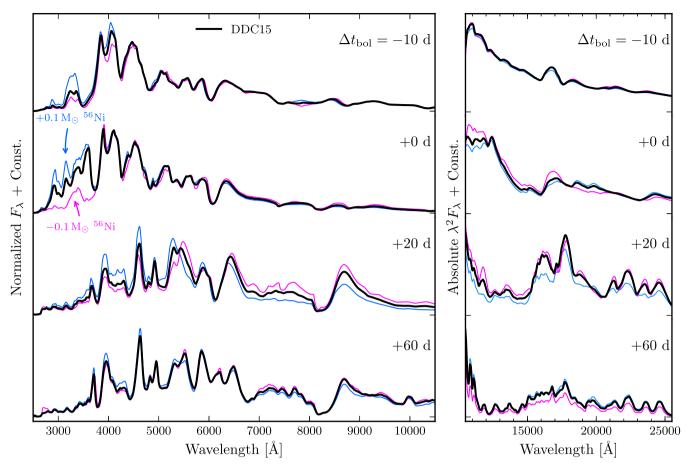
Figure 10. Illustration of the impact of a $\pm 0.1\,M_\odot$ variation in ^{56}Ni mass (coloured curves) with respect to our reference model DDC15 (black) on the optical (left) and NIR (right) spectra at four selected times between -10 and $+60$ d from bolometric maximum. The optical spectra have been normalized to the same mean flux in the range 5000–6500 Å to better visualize relative differences in the SED. The NIR spectra on the other hand are not normalized (but the flux has been scaled by λ^2 for better visibility), such that differences between the models correspond to real variations in absolute flux. The tick marks on the ordinate give the zero-flux level. Notice the lower flux level in the near-UV relative to the optical in our model with *less* ^{56}Ni.

the similar density structure and ^{56}Ni distribution of the inner ejecta in our three Chandrasekhar-mass models.

The spectra are remarkably similar at these times, with minor differences in SED confined to $\lesssim 6000$ Å, owing to the more uniform ionization state of IGEs. Variations in Cr II line opacity continue to affect the flux around 5300 Å. Although not apparent in Fig. 10 due to the flux normalization, the [Co III] 5888 Å emission strength correlates with ^{56}Ni mass. This correlation is also present in observations of SNe Ia and supports the association of this feature with cobalt (see Dessart et al. 2014a, and references therein).

7.4 NIR homogeneity and secondary maxima

An increase in ^{56}Ni mass causes an earlier hardening of the SED and a delayed cooling of the ejecta. The result is an earlier decline (and hence an earlier first maximum) in the NIR bands (Table 3).

The associated delayed III→II recombination of IGEs has a stronger impact in the bluest bands, resulting in a larger magnitude variation amongst our three models compared to redder optical and NIR bands (Fig. 11; see also B13, Appendix C). The variation in the *I*, *J*, and K_s magnitudes is less than 0.1 mag (and occasionally less than 0.05 mag) between the epoch of first maximum in those bands up until ~10 d past bolometric maximum. Such a small
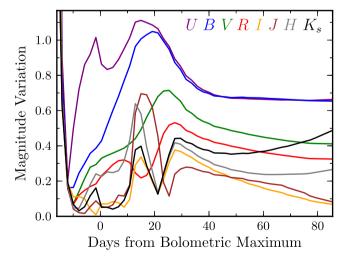

Figure 11. Evolution of the magnitude variation in various bands amongst our three models, spanning ~0.2 $M_\odot$ in ^{56}Ni mass.

intrinsic dispersion (also reflected in the uniformity of their spectra; see Fig. 10) confirms the potential of NIR photometry of SNe Ia for accurate distance determinations (e.g. Krisciunas, Phillips & Suntzeff 2004b).
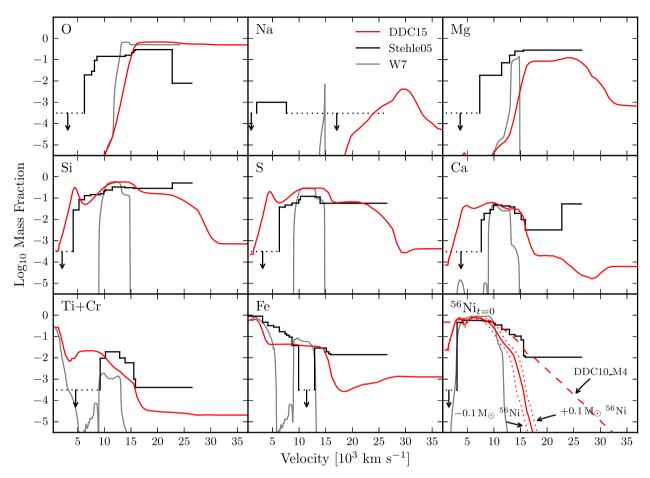
Figure 12. Comparison of abundance profiles in our reference model DDC15 (red, solid line) with those derived via spectroscopic modelling by Stehle et al. (2005) [black; the data were manually scanned from their fig. 5 a] and the W7 model of Nomoto et al. (1984) [grey]. The ^{56}Ni distribution is shown at $t_{exp} \approx 0$. Since the ordinate of fig. 5(a) of Stehle et al. (2005) does not extend below $\sim 3.1 \times 10^{-4}$, we give upper limits as dotted lines plus a downward-pointing arrow. We also show the ^{56}Ni distribution for our models with ± 0.1 M$_\odot$ of ^{56}Ni (red dotted lines), and for a mixed version of our model with $+0.1$ M$_\odot$ of ^{56}Ni (noted DDC10_M4 in D14b; red dashed line). The abundances for Mg through Fe are solar beyond $\sim 35\,000$ km s^{-1} in our model.

The same effect delays the time of NIR secondary maxima for larger ^{56}Ni mass (see also Kasen 2006), but leaves their magnitude unchanged (Table 3), in agreement with observations (Biscardi et al. 2012, their fig. 8). The result is a larger magnitude variation in the NIR range at 15–20 d from bolometric maximum, even exceeding that in the V and R bands.

7.5 IGE abundance and near-UV flux level

The ± 0.1 M$_\odot$ variation in ^{56}Ni mass represents a non-negligible variation in the relative abundances of IGEs and IMEs[3] (see Table 1), which often result in a modest impact on the predicted observables, illustrating the degeneracy of SN Ia properties and the difficulties associated with abundance determinations in these events (see next section).

Part of this degeneracy results from variations in ionization whose impact often supersedes those associated with variations in abundance in determining the ejecta opacity. In the near-UV range, where most of the opacity is due to IGEs, it is our model with *less* ^{56}Ni (and hence less IGEs) that has the lowest near-UV flux level relative

---

[3] Since all but $\lesssim 0.01$ M$_\odot$ of the progenitor WD is burnt in our delayed-detonation models, the ± 0.1 M$_\odot$ variation in ^{56}Ni mass results in a comparable variation (of opposite sign) in IME mass.

to the optical up until maximum light (Fig. 10), due to the lower ionization level of Ni/Co/Fe. Our models thus show that an increase in the IGE abundance in SNe Ia does not necessarily result in more opaque ejecta (see also Sauer et al. 2008), which complicates the use of near-UV spectra to constrain the progenitor metallicity (see e.g. Foley & Kirshner 2013).

The larger sensitivity of the U-band flux to the mass of ^{56}Ni results in a $\lesssim 1$ mag variation in this band amongst our three models around maximum light (Fig. 11), and a larger variation in $U - V$ compared to other colour indices (Fig. 6), in line with observational findings (e.g. Jha et al. 2006). This large variation could significantly affect reddening determinations of SNe Ia.

8 COMPARISON TO PREVIOUS WORK

In-depth studies of SN 2002bo have been presented by Benetti et al. (2004) and Stehle et al. (2005). The latter study attempts to infer the chemical stratification of the SN 2002bo ejecta based on steady-state spectroscopic modelling under the assumption of a sharp photosphere emitting a pure thermal continuum. Stehle et al. assume an ejecta structure (the density profile of W7 shown in Fig. 2) and vary the abundances in order to reproduce the observed spectra at selected epochs. Their abundance profiles are shown in Fig. 12. For comparison, we overplot the abundance profiles for our

Table 4. Comparison of nucleosynthetic yields at $t_{exp} \approx 0$.

Species	DDC15 ($M_\odot$)	Stehle05 ($M_\odot$)	W7 ($M_\odot$)
^{56}Ni	0.511	0.520	0.587
Fe^a	0.100	0.360	0.145
Ti+Cr	0.018	0.003	0.005
Ca	0.045	0.020	0.012
S	0.197	0.067	0.085
Si	0.306	0.220	0.154
Mg	0.011	0.080	0.013
Na	1.68($-$5)	0.001	6.32($-$5)
O	0.105	0.110	0.138
C	0.003	$\lesssim$0.002	0.047

Notes. Numbers in parenthesis correspond to powers of 10.
^{a}Stable isotopes only (^{54}Fe, ^{56}Fe, ^{57}Fe, and ^{58}Fe). Since these yields are given at $t_{exp} \approx 0$, the stable iron yield does not include ^{56}Fe from ^{56}Ni decay.

model DDC15 and those of W7. The elemental yields are reported in Table 4. We discuss in turn the inferred chemical stratification and the validity of a diffusive inner boundary, which is a fundamental ansatz of the method applied by Stehle et al. (2005).

8.1 Chemical stratification

The most striking difference of our results with those of Stehle et al. (2005) is that they require a large overabundance of IGEs and IMEs in the outer layers ($\gtrsim$15 000 km s^{-1}) in order to reproduce the broad lines of SN 2002bo, including the blue wings of Fe II 4800 Å at early times. Although our models possess $\sim$1000 times less Ca (by mass) beyond $\sim$20 000 km s^{-1}, the resulting synthetic spectra exhibit high-velocity Ca II features. Such a huge difference illustrates the difficulties associated with some abundance determinations that are highly sensitive to the ionization balance and outer density structure.

In the intermediate layers (10 000–15 000 km s^{-1}) the distribution of IMEs is in good agreement with our model, although Stehle et al. (2005) infer a larger Mg abundance (0.08 $M_\odot$ cf. $\sim$0.01 $M_\odot$ in our model) in order to reproduce the Mg II absorption feature around 4200 Å in the early-time spectra. Past maximum light, however, the deep absorption at $\sim$4400 Å is caused by several Fe II lines in our model, not by Mg II, hence we can reproduce this feature despite the sharp drop in Mg abundance below $\sim$15 000 km s^{-1}. Stehle et al. (2005) also argue for significant downward mixing of oxygen ($X_O \gtrsim 0.1$ above $\sim$8500 km s^{-1}), when we satisfactorily fit the O I 7773 Å feature up until shortly after maximum light with no oxygen present below $\sim$10 000 km s^{-1}.

Contrary to our model, Stehle et al. (2005) infer the presence of Na and the absence of Ti/Cr below $\sim$10 000 km s^{-1}. For Na, their abundance constraint is most likely a misidentification of the emission feature at $\sim$5900 Å past maximum light, which is due to [Co III] 5888 Å, not Na I (see Dessart et al. 2014a). As for Ti/Cr, several Cr II lines affect the flux level around $\sim$5300 Å past maximum light (Section 6.3), so that chromium must be present in the inner ejecta.[4]

The ^{56}Ni distribution in our model is comparable to that inferred by Stehle et al. (2005) in the range 5000–10 000 km s^{-1}, but drops more rapidly beyond 10 000 km s^{-1}. With our distribution we reproduce the early rise in bolometric luminosity (Fig. 4). Nonetheless, we argued for some additional outward mixing of ^{56}Ni based on the lack of absorption in the blue wings of several features in the early-time spectra (Section 6.1). In fact, the ^{56}Ni distribution of the mixed model DDC10_M4 of D14b closely matches the ^{56}Ni distribution of Stehle et al. (2005). Note that we cannot really comment on the distribution below $\sim$3000 km s^{-1} since we did not evolve our model beyond $\sim$100 d past explosion, when most of the flux is expected to emerge from the inner $\sim$0.1 $M_\odot$ of ejecta.

8.2 The validity of a diffusive inner boundary

When modelling the early-time spectra of SN 2002bo Stehle et al. (2005) assume there exists a sharp photosphere at a predefined velocity emitting a thermal continuum, yet the importance of line scattering in SNe Ia leads to strong departures from local thermodynamic equilibrium (LTE) in both the gas (level populations) and the radiation field (mean intensity J_ν). In our simulations, we solve the non-LTE time-dependent radiative transfer for the whole ejecta, with a zero-flux inner boundary condition at the base of the innermost ejecta shell. We can thus check how J_ν and B_ν deviate from each other as function of time since explosion, and as a function of depth in the ejecta. In Fig. 13 we illustrate the departures of the mean intensity from a Planckian distribution based on our non-LTE time-dependent radiative transfer calculations with CMFGEN for model DDC15 around bolometric maximum.

In the innermost regions, at a Rosseland-mean optical depth $\tau_{Ross} \gtrsim 100$ ($v \lesssim 1500$ km s^{-1}), we have $J_\nu \approx B_\nu(T)$ at all UV, optical, and NIR wavelengths. Hence, the non-LTE solver recovers LTE conditions, i.e. the radiation and the gas are in equilibrium at the same (local) temperature T. At $\tau_{Ross} \approx 30$ ($v \approx 3500$ km s^{-1}), $J_\nu < B_\nu(T)$ in the red part of the optical and in the NIR, but the radiation is still Planckian below $\sim$5000 Å, where the large number of lines ensures an efficient thermalization. As we progress further out to τ_{Ross} of 10 and 1 ($\sim$6000 and $\sim$11 000 km s^{-1}, respectively), J_ν drops below $B_\nu(T)$ even in the UV, although the SED remains smooth below $\sim$2500 Å. This persists out to $\tau_{Ross} \approx 0.1$ ($v \approx 16 000$ km s^{-1}), although $B_\nu(T)$ is then no longer a good representation of J_ν.

Thus, already at an optical depth of several tens, injecting photons with a Planckian distribution would lead to an overestimate of the flux in the red part of the spectrum. The situation is even worse when only the outermost (optically thin) ejecta are treated and one assumes a sharp blackbody emitting photosphere at $\tau \approx 1$, as done by Stehle et al. (2005). As a result, they invoke a lower reddening for SN 2002bo than that inferred from observational constraints. In contrast, our full non-LTE solution treats the entire ejecta and yields a satisfactory match to the overall SED at all times with a total reddening $E(B - V) = 0.41$ mag (Figs 8 and 9).

9 DISCUSSION AND CONCLUSION

We have presented a detailed analysis of the photometric and spectroscopic evolution of a 1D Chandrasekhar-mass delayed-detonation model for the Type Ia SN 2002bo. Beyond providing

---

[4] At the time their paper was written, Stehle et al. (2005) did not have access to any spectra of SN 2002bo between +6 and +263 d past *B*-band maximum,

and thus could provide only weak constraints on the abundance distribution in these intermediate ejecta layers.

Figure 13. Illustration of the wavelength dependence of the mean intensity J_ν (solid lines) and the Planck function B_ν (dotted lines) at different depths in the ejecta for model DDC15 at -2.1 d from bolometric maximum. From top to bottom, the panels correspond to locations from the inner to the outer ejecta. For each location, we give the velocity, the Rosseland-mean optical depth, and the gas temperature. As the optical depth decreases, J_ν deviates more and more from $B_\nu(T)$.

a suitable model for this event, it provides a reference for understanding all SNe Ia similar to that prototype.

The good match we obtain with the light curves and spectra over the first $\sim$100 d since explosion gives some support to the standard single-degenerate model for these objects. It remains to be studied whether WD–WD merger models (e.g. Pakmor et al. 2012) can reproduce events like SN 2002bo as well as delayed detonations of single WDs at the Chandrasekhar mass. The ejected mass distribution of SNe Ia found by Scalzo, Ruiter & Sim (2014) is strongly peaked at $\sim$1.4 M$_\odot$, yet reveals a significant fraction of sub-Chandrasekhar-mass progenitors, although these are associated with the least luminous events. While it is unclear to what extent

a direct confrontation to observations reveals the successes and shortcomings either of the radiative transfer treatment or of the underlying explosion model (or both), a proper assessment requires treating the entire SN ejecta in non-LTE at all times (see Section 8.2).

Our assumption of spherical symmetry and our somewhat artificial treatment of the delayed-detonation mechanism are not detrimental to reproducing the radiative properties of a prototypical SN Ia. The mild disagreement between our model and SN 2002bo at the earliest times may be resolved by invoking a greater outward mixing of ^{56}Ni, but could also indicate some fundamental characteristic of the explosion not captured by our artificial, 1D set-up.

In B13 we noted a general overestimate of the width of the characteristic Si II 6355 Å line in our models to account for the bulk of normal SNe Ia. While this was originally flagged as a potential overestimate of the kinetic energy in our input 1D hydrodynamical models, it has since then become clear that the observed diversity in spectral line widths could reflect profound physical differences in the explosion mechanism (in particular, pulsating delayed detonations result in a narrower Si II 6355 Å line; see D14b). The delayed-detonation models discussed in B13 are thus well suited to broad-lined SNe Ia.

The observed paucity of C II lines in the early-time spectra of broad-lined SNe Ia is then physical and not related, for example, to line overlap. In the pulsating delayed-detonation models of D14b, carbon is present down to $\sim$15 000 km s^{-1}, close to the spectrum-formation region at early times. C II lines are thus predicted in these models, along with a narrower Si II 6355 Å line profile. The preferential association of C II detections with narrow-lined SNe Ia (termed 'core normal' by Branch et al. 2006) is backed up by extensive data sets (e.g. Parrent et al. 2011).

We show that ± 0.1 M$_\odot$ variations in ^{56}Ni mass have a modest impact on the bolometric and colour evolution of our model. Spectroscopically, most of the effect is seen blueward of $\sim$3500 Å up until maximum light, our model with less ^{56}Ni displaying a lower near-UV flux level despite the lower abundance of IGEs. In the NIR, an increase in ^{56}Ni mass delays the secondary maxima but does not affect their magnitude, as found in observational studies. More importantly, our models confirm the homogeneous nature of SNe Ia in the NIR, with a $<$0.1 mag variation in the I, J, and K_s bands around maximum light.

Allowing for homologous expansion of the ejecta inherited from the hydrodynamical modelling of the explosion, combined with a self-consistent time-dependent radiative transfer treatment, our models yield a better match to SN 2002bo than previous parametrized approaches. The complex nature of the radiative transfer problem (line overlap, line saturation, uncertain ionization, scattering versus absorption, non-thermal processes, etc.) does not permit a direct and accurate determination of elemental abundances. Instead, a global modelling of the ejecta to predict simultaneously the bolometric and multiband light curves, as well as the optical and NIR spectra, allows a better assessment of the adequacy of a given model.

ACKNOWLEDGEMENTS

REFERENCES

Badenes C., Maoz D., 2012, ApJ, 749, L11
Baron E., Höflich P., Krisciunas K., Dominguez I., Khokhlov A. M., Phillips M. M., Suntzeff N., Wang L., 2012, ApJ, 753, 105
Benetti S. et al., 2004, MNRAS, 348, 261
Benetti S. et al., 2005, ApJ, 623, 1011
Bessell M. S., 1990, PASP, 102, 1181
Biscardi I. et al., 2012, A&A, 537, A57
Blondin S. et al., 2012, AJ, 143, 126
Blondin S., Dessart L., Hillier D. J., Khokhlov A. M., 2013, MNRAS, 429, 2127 (B13)
Branch D. et al., 2006, PASP, 118, 560
Cardelli J. A., Clayton G. C., Mathis J. S., 1989, ApJ, 345, 245
Childress M. J., Filippenko A. V., Ganeshalingam M., Schmidt B. P., 2014, MNRAS, 437, 338
Cohen M., Wheaton W. A., Megeath S. T., 2003, AJ, 126, 1090
Dessart L., Hillier D. J., Blondin S., Khokhlov A., 2014a, MNRAS, 439, 3114
Dessart L., Blondin S., Hillier D. J., Khokhlov A., 2014b, MNRAS, 441, 532 (D14b)
Dessart L., Hillier D. J., Blondin S., Khokhlov A., 2014c, MNRAS, 441, 3249 (D14c)
Domínguez I., Höflich P., Straniero O., 2001, ApJ, 557, 279
Foley R. J., Kirshner R. P., 2013, ApJ, 769, L1
Friesen B., Baron E., Wisniewski J. P., Parrent J. T., Thomas R. C., Miller T. R., Marion G. H., 2014, ApJ, 792, 120
Hillier D. J., 1990, A&A, 231, 116
Hillier D. J., Dessart L., 2012, MNRAS, 424, 252
Höflich P., Gerardy C. L., Fesen R. A., Sakai S., 2002, ApJ, 568, 791
Hoyle F., Fowler W. A., 1960, ApJ, 132, 565
Jha S. et al., 2006, AJ, 131, 527
Kasen D., 2006, ApJ, 649, 939
Khokhlov A., Müller E., Höflich P., 1993, A&A, 270, 223
Krisciunas K. et al., 2004a, AJ, 128, 3034
Krisciunas K., Phillips M. M., Suntzeff N. B., 2004b, ApJ, 602, L81

Kuchner M. J., Kirshner R. P., Pinto P. A., Leibundgut B., 1994, ApJ, 426, L89
Lentz E. J., Baron E., Branch D., Hauschildt P. H., Nugent P. E., 2000, ApJ, 530, 966
Ng K.-C., 1974, J. Chem. Phys., 61, 2680
Nomoto K., Thielemann F.-K., Yokoi K., 1984, ApJ, 286, 644
Nugent P. E. et al., 2011, Nature, 480, 344
Pakmor R., Kromer M., Taubenberger S., Sim S. A., Röpke F. K., Hillebrandt W., 2012, ApJ, 747, L10
Parrent J. T. et al., 2011, ApJ, 732, 30
Pinto P. A., Eastman R. G., 2000, ApJ, 530, 757
Piro A. L., Nakar E., 2014, ApJ, 784, 85
Sauer D. N. et al., 2008, MNRAS, 391, 1605
Scalzo R. A., Ruiter A. J., Sim S. A., 2014, MNRAS, 445, 2535
Silverman J. M. et al., 2012, MNRAS, 425, 1789
Stehle M., Mazzali P. A., Benetti S., Hillebrandt W., 2005, MNRAS, 360, 1231
van Kerkwijk M. H., Chang P., Justham S., 2010, ApJ, 722, L157
Wang X. et al., 2009, ApJ, 699, L139
Zheng W. et al., 2013, ApJ, 778, L15

APPENDIX A: CONVERGENCE

CMFGEN employs an iterative method for solving the statistical and radiative equilibrium equations (see Hillier 1990). A model is converged when the maximum correction to any of the variables involved (temperature, electron density, and level populations) at all depths falls below some predefined value set by the EPS_TERM parameter (typically <0.1 per cent). The vast majority of corrections are well below this limit.

We illustrate the convergence properties of our DDC15 model in Fig. A1, at four selected time steps and for four different ejecta locations. We only show the temperature, since its rate of convergence largely determines the global convergence properties of the model. Since small corrections to the temperature can result in potentially large corrections of the level populations, the temperature corrections are orders of magnitude less than EPS_TERM by the time convergence is achieved (typically in 40–70 iterations).

After the first iteration, the temperature is set to that obtained via a grey calculation, and the fractional change is with respect to the converged solution of the previous time step, hence the potentially large correction (∼10 per cent) associated with the first datum. The temperature is then held fixed (i.e. the temperature correction is zero) during a series of Λ and full iterations in order to stabilize the corrections to the level populations (see Hillier & Dessart 2012). Sharp variations in the temperature correction result from Ng accelerations (Ng 1974), used periodically to increase the convergence rate. Various diagnostics, such as electron energy balance, global energy conservation, and ionization equilibrium, are available as independent checks of the convergence.

APPENDIX B: BOLOMETRIC LUMINOSITY AND ABSOLUTE MAGNITUDES

Table B1 lists the bolometric and pseudo-bolometric ($U \rightarrow K_s$) luminosities, as well as the optical–NIR absolute magnitudes of model DDC15 as a function of time since explosion.

Figure A1. Illustration of the temperature convergence at four selected time steps in our model sequence (increasing from top to bottom). At each time, we show the fractional change in temperature $|\Delta T|/T = 100 \times |T_{i-1} - T_i|/T_{i-1}$ versus iteration number i, at four different ejecta locations: In the inner, ^{56}Ni-deficient region ($v \approx 2000$ km s^{-1}); in the ^{56}Ni-rich layers ($v \approx 7000$ km s^{-1}); in the IME-rich layers ($v \approx 12\,000$ km s^{-1}); in the outer C/O-dominated layers ($v \approx 30\,000$ km s^{-1}). The symbols indicate the sign of the correction (positive for filled upward-pointing triangles; negative for open downward-pointing triangles). The dotted line in each plot corresponds to the value of the convergence criterion, noted EPS_TERM in CMFGEN. It is set to 0.04 per cent at all time steps shown here, except at $t_{\rm exp} = 40.11$ d where it is set to 0.07 per cent.

Table B1. Bolometric luminosity, pseudo-bolometric ($U \to K_s$) luminosity, and optical–NIR absolute magnitudes for model DDC15.

t_{exp} (d)	L_{bol} (erg s^{-1})	$L_{U \to K_s}$ (erg s^{-1})	U (mag)	B (mag)	V (mag)	R (mag)	I (mag)	J (mag)	H (mag)	K_s (mag)
0.98	6.02(39)	4.98(39)	−5.64	−7.79	−9.85	−11.26	−11.22	−12.43	−12.47	−12.65
1.07	8.71(39)	7.37(39)	−5.68	−8.40	−10.45	−11.77	−11.67	−12.74	−12.80	−12.93
1.18	1.27(40)	1.10(40)	−6.11	−9.00	−11.05	−12.27	−12.14	−13.05	−13.12	−13.22
1.30	1.84(40)	1.63(40)	−6.65	−9.61	−11.62	−12.74	−12.61	−13.36	−13.44	−13.52
1.43	2.62(40)	2.37(40)	−7.38	−10.26	−12.16	−13.14	−13.01	−13.65	−13.75	−13.82
1.57	3.69(40)	3.37(40)	−8.28	−10.91	−12.68	−13.52	−13.37	−13.95	−14.05	−14.11
1.73	5.15(40)	4.72(40)	−9.24	−11.54	−13.16	−13.87	−13.71	−14.24	−14.33	−14.39
1.90	7.06(40)	6.48(40)	−10.13	−12.11	−13.60	−14.18	−14.01	−14.51	−14.60	−14.65
2.09	9.65(40)	8.85(40)	−10.93	−12.63	−14.03	−14.48	−14.31	−14.78	−14.87	−14.93
2.30	1.31(41)	1.20(41)	−11.61	−13.11	−14.42	−14.76	−14.61	−15.06	−15.14	−15.20
2.53	1.76(41)	1.60(41)	−12.23	−13.55	−14.79	−15.04	−14.89	−15.33	−15.40	−15.46
2.78	2.33(41)	2.13(41)	−12.84	−13.98	−15.11	−15.32	−15.16	−15.59	−15.64	−15.72
3.06	3.11(41)	2.84(41)	−13.43	−14.40	−15.43	−15.60	−15.43	−15.86	−15.89	−15.98
3.37	4.17(41)	3.83(41)	−14.01	−14.84	−15.74	−15.89	−15.70	−16.13	−16.15	−16.24
3.70	5.67(41)	5.20(41)	−14.57	−15.29	−16.06	−16.20	−15.99	−16.42	−16.42	−16.51
4.07	7.63(41)	7.05(41)	−15.07	−15.73	−16.35	−16.49	−16.26	−16.68	−16.68	−16.76
4.48	1.02(42)	9.50(41)	−15.54	−16.17	−16.64	−16.78	−16.53	−16.95	−16.93	−16.99
4.93	1.36(42)	1.27(42)	−15.99	−16.58	−16.91	−17.06	−16.79	−17.19	−17.16	−17.21
5.42	1.78(42)	1.67(42)	−16.43	−16.96	−17.16	−17.33	−17.04	−17.43	−17.37	−17.39
5.96	2.32(42)	2.19(42)	−16.87	−17.31	−17.41	−17.58	−17.30	−17.64	−17.56	−17.56
6.56	2.98(42)	2.83(42)	−17.31	−17.63	−17.64	−17.82	−17.58	−17.83	−17.73	−17.70
7.22	3.78(42)	3.60(42)	−17.72	−17.92	−17.85	−18.04	−17.84	−17.99	−17.87	−17.83
7.94	4.70(42)	4.48(42)	−18.09	−18.17	−18.06	−18.25	−18.07	−18.14	−17.98	−17.93
8.73	5.70(42)	5.42(42)	−18.39	−18.39	−18.25	−18.43	−18.25	−18.26	−18.06	−18.00
9.60	6.74(42)	6.40(42)	−18.65	−18.59	−18.43	−18.59	−18.40	−18.36	−18.10	−18.05
10.56	7.80(42)	7.40(42)	−18.88	−18.76	−18.60	−18.73	−18.52	−18.43	−18.12	−18.06
11.62	8.78(42)	8.34(42)	−19.04	−18.89	−18.75	−18.86	−18.62	−18.51	−18.13	−18.07
12.78	9.63(42)	9.22(42)	−19.15	−19.01	−18.88	−18.97	−18.67	−18.53	−18.10	−18.04
14.06	1.05(43)	9.90(42)	−19.31	−19.10	−18.97	−19.05	−18.72	−18.53	−18.04	−17.98
15.47	1.09(43)	1.05(43)	−19.36	−19.14	−19.05	−19.12	−18.74	−18.50	−17.99	−17.94
17.02	1.16(43)	1.08(43)	−19.42	−19.14	−19.17	−19.17	−18.83	−18.45	−17.98	−18.07
18.72	1.13(43)	1.07(43)	−19.31	−19.12	−19.21	−19.19	−18.83	−18.35	−17.94	−18.05
20.59	1.08(43)	1.03(43)	−19.18	−19.07	−19.23	−19.19	−18.81	−18.24	−17.95	−18.06
22.65	1.00(43)	9.70(42)	−19.02	−18.99	−19.21	−19.16	−18.77	−18.09	−18.00	−18.08
24.91	9.01(42)	8.72(42)	−18.82	−18.85	−19.16	−19.08	−18.70	−17.81	−18.06	−18.11
27.40	7.76(42)	7.51(42)	−18.57	−18.65	−19.05	−18.95	−18.59	−17.33	−18.09	−18.13
30.14	6.56(42)	6.36(42)	−18.29	−18.39	−18.89	−18.79	−18.52	−17.05	−18.18	−18.17
33.15	5.74(42)	5.54(42)	−17.83	−17.97	−18.70	−18.70	−18.72	−17.34	−18.62	−18.54
36.46	5.14(42)	4.93(42)	−17.43	−17.58	−18.47	−18.61	−18.85	−17.61	−18.80	−18.70
40.11	4.47(42)	4.15(42)	−17.05	−17.18	−18.17	−18.45	−18.83	−17.92	−18.80	−18.70
44.12	3.51(42)	3.28(42)	−16.75	−16.86	−17.85	−18.17	−18.58	−17.76	−18.53	−18.41
48.53	2.74(42)	2.56(42)	−16.50	−16.61	−17.59	−17.91	−18.30	−17.35	−18.22	−18.05
53.38	2.20(42)	2.05(42)	−16.31	−16.42	−17.38	−17.69	−18.03	−16.92	−17.92	−17.72
58.72	1.80(42)	1.67(42)	−16.15	−16.27	−17.20	−17.49	−17.76	−16.50	−17.64	−17.43
64.59	1.48(42)	1.37(42)	−16.00	−16.14	−17.03	−17.30	−17.49	−16.08	−17.37	−17.15
71.05	1.22(42)	1.13(42)	−15.84	−16.02	−16.85	−17.10	−17.21	−15.65	−17.09	−16.87
78.16	1.00(42)	9.29(41)	−15.68	−15.90	−16.66	−16.89	−16.94	−15.20	−16.80	−16.59
86.00	8.15(41)	7.56(41)	−15.49	−15.77	−16.45	−16.65	−16.66	−14.74	−16.48	−16.29
94.60	6.57(41)	6.10(41)	−15.29	−15.63	−16.23	−16.39	−16.38	−14.26	−16.12	−15.98
104.10	5.26(41)	4.86(41)	−15.05	−15.48	−15.98	−16.10	−16.10	−13.81	−15.73	−15.66

Note. Numbers in parentheses correspond to powers of 10. *UBVRI* magnitudes are based on the passbands of Bessell (1990); *JHK*$_s$ magnitudes are in the 2MASS system (Cohen, Wheaton & Megeath 2003).

APPENDIX C: STRONG LINES

In Tables C1–C15 we report the strongest lines in the optical (3000–10 000 Å) and NIR (1–2.5 μm) ranges at a given time between 4.1 and 104.1 d past explosion (−13.5 and +86.5 d from bolometric maximum). A line is considered strong when its absolute Sobolev equivalent width (EW) exceeds 10 per cent of the largest absolute EW within $\pm10^4$ km s^{-1} of the line's central wavelength. Forbidden and semiforbidden transitions are noted using the appropriate brackets around the line wavelength (in air). We highlight transitions connected to the ground state with a '†' symbol.

These tables are meant to serve as a guide for line identification in spectra of SNe Ia similar to SN 2002bo. However, we caution the reader that the Sobolev EWs are only approximate and neglect important effects such as line overlap. Moreover, lines with a P-Cygni profile morphology may be important contributors to the resulting spectrum yet yield a small absolute EW. This explains for instance why the strong Ca II K line (3934 Å) does not show up in Table C2 ($t_{exp} = 5.4$ d) where Fig. D1 shows the strong impact of the Ca II H&K feature on the optical spectra at these times, and the Ca II K line indeed appears in Tables C1 ($t_{exp} = 4.1$ d) and C3 ($t_{exp} = 9.6$ d).

Table C1. Strong lines in the optical and NIR at 4.1 d past explosion.

| | $t_{exp} = 4.1$ d ($\Delta t_{bol} = -13.5$ d) | |
| | 3000–10 000 Å | 1.0–2.5 μm |
Ion	λ_{air} (Å)	λ_{air} (μm)
O I	9266.01	1.316
Mg II	7896.37	1.009
		1.091
		1.863
		2.137
		2.404
Al II	7042.08	1.008
Si II	5978.93	1.175
	6347.11	1.370
	9412.63	1.445
		1.691
		1.947
Si III	4828.95	1.250
	5739.73	
S II	4162.67	1.523
S III	6755.65	. . .
	7171.58	
Ar II	4348.06	. . .
Ca II	3933.66†	1.184
	8542.09	
Ti II	3088.04	. . .
	3234.52	
	3349.41	
	3759.30	
Cr II	3124.97	. . .
Fe II	3002.65	. . .
Fe III	4419.60	. . .
	5156.11	
Co II	3501.72	. . .
Ni II	3513.99	. . .

Table C2. Strong lines in the optical and NIR at 5.4 d past explosion.

| | $t_{exp} = 5.4$ d ($\Delta t_{bol} = -12.1$ d) | |
| | 3000–10 000 Å | 1.0–2.5 μm |
Ion	λ_{air} (Å)	λ_{air} (μm)
O I	7771.94	1.316
Mg II	7896.37	1.091
		1.863
		2.137
		2.404
Al II	7042.08	1.008
Si II	5978.93	1.175
	6347.11	1.370
	9412.63	1.445
		1.691
Si III	4552.62	1.250
	4828.95	1.502
	5739.73	
	7466.32	
	8262.57	
	9799.91	
S II	5453.85	1.318
S III	3497.28	1.032
	3838.27	
	4253.50	
	5219.31	
	6755.65	
	7171.58	
Ar II	4806.02	. . .
Ca II	8542.09	1.856
Sc II	3572.53	. . .
Ti II	3088.04	. . .
	3234.52	
Cr II	3124.97	. . .
Fe II	3002.65	. . .
Fe III	5156.11	. . .
Ni II	3087.07	. . .

Table C3. Strong lines in the optical and NIR at 9.6 d past explosion.

| | $t_{exp} = 9.6$ d ($\Delta t_{bol} = -8.0$ d) | |
| | 3000–10 000 Å | 1.0–2.5 μm |
Ion	λ_{air} (Å)	λ_{air} (μm)
O I	7771.94	1.316
Mg II	9218.25	1.091
Si II	6347.11	1.370
		1.691
		2.199
Si III	4552.62	1.134
	4828.95	1.250
	5739.73	1.502
	7466.32	2.093
	8262.57	
	9323.89	
	9799.91	
Si IV	6701.21	1.190
	7720.37	1.855
	8957.25	1.985
		2.426
S II	5453.85	1.318
S III	3234.01	1.032
	3497.28	1.421
	4253.50	
	5219.31	
S IV	6140.66	. . .
	7003.27	
Ar II	4806.02	. . .
Ar III	7988.48	1.312
Ca II	3933.66†	1.856
	8542.09	
Ti II	3349.41	. . .
Cr II	3124.97	. . .
Fe II	5169.03	. . .
Fe III	3013.13	. . .
Co II	3501.72	. . .
Co III	3010.88	. . .
Ni II	3513.99	. . .

Table C4. Strong lines in the optical and NIR at 12.8 d past explosion.

| | $t_{exp} = 12.8$ d ($\Delta t_{bol} = -4.8$ d) | |
| | 3000–10 000 Å | 1.0–2.5 μm |
Ion	λ_{air} (Å)	λ_{air} (μm)
O I	7771.94	. . .
Mg II	9218.25	1.091
Si II	5978.93	1.370
	6347.11	1.691
		2.199
Si III	4552.62	1.134
	5739.73	1.250
	7466.32	1.502
	8262.57	2.093
	9323.89	
Si IV	6701.21	1.190
	7720.37	1.855
	8957.25	1.985
		2.426
S II	4815.55	1.362
	5453.85	
S III	3497.28	1.032
	4253.50	1.421
	5219.31	
S IV	7003.27	. . .
Ar II	4806.02	. . .
Ar III	[7135.79]†	1.312
Ca II	3933.66†	1.856
	8542.09	
Ti II	3349.41	. . .
Cr II	3124.97	. . .
Fe II	5169.03	. . .
Fe III	3013.13	. . .
Co II	3501.72	2.221
Co III	3010.88	[2.281]
	3305.27	
Co IV	8033.21	. . .
Ni II	3513.99	. . .

Table C5. Strong lines in the optical and NIR at 15.5 d past explosion.

| Ion | $t_{exp} = 15.5$ d ($\Delta t_{bol} = -2.1$ d) | |
	3000–10 000 Å λ_{air} (Å)	1.0–2.5 μm λ_{air} (μm)
O I	7771.94	...
Mg II	9218.25	1.091
Si II	6347.11	1.691
		2.199
Si III	4552.62	1.134
	5739.73	1.250
	7466.32	1.502
	9323.89	
Si IV	6701.21	1.190
	7720.37	1.855
		2.426
S II	5453.85	1.362
S III	3497.28	1.032
	4253.50	1.421
	5219.31	
S IV	7003.27	...
Ar II	4806.02	1.047
Ar III	[7135.79]†	1.440
Ca II	3933.66†	1.856
	8542.09	
Ti II	3349.41	...
Cr II	3124.97	...
Fe II	5169.03	...
Fe III	3013.13	...
Fe IV	...	1.868
Co II	3501.72	2.221
Co III	3010.88	[2.002]
	3305.27	[2.097]
	4740.66	[2.281]
Co IV	8033.21	...
Ni II	3513.99	...
Ni III	4874.95	...

Table C6. Strong lines in the optical and NIR at 17.0 d past explosion.

| Ion | $t_{exp} = 17.0$ d ($\Delta t_{bol} = -0.5$ d) | |
	3000–10 000 Å λ_{air} (Å)	1.0–2.5 μm λ_{air} (μm)
O I	7771.94	...
Mg II	7896.37	1.091
Si II	6347.11	1.175
		1.370
		1.691
		2.199
Si III	4552.62	1.134
	5739.73	1.250
	7466.32	
	9323.89	
S II	5453.85	1.362
S III	3497.28	1.032
	4253.50	1.421
	5219.31	2.374
	6755.65	
Ar II	4806.02	1.047
Ar III	[7135.79]†	1.312
Ca II	3933.66†	1.885
	8542.09	
Cr II	3124.97	...
Fe II	5169.03	...
Fe III	5156.11	[2.218]
Co II	3501.71	1.777
Co III	3010.88	[1.548]
	3305.27	[2.002]
	4740.66	[2.097]
	5544.79	[2.281]
	6078.55	[2.473]
Ni II	3513.99	...
Ni III	[7889.93]	1.001

Table C7. Strong lines in the optical and NIR at 22.6 d past explosion.

| | $t_{exp} = 22.6$ d ($\Delta t_{bol} = +5.1$ d) | |
| | 3000–10 000 Å | 1.0–2.5 μm |
Ion	λ_{air} (Å)	λ_{air} (μm)
O I	7771.94	. . .
Mg II	9218.25	1.091
Si II	6347.11	1.175
		1.445
		1.691
Si III	5739.73	1.134
	9323.89	1.250
S II	5453.85	[1.032]
S III	4253.50	1.087
Ar II	6643.69	. . .
Ar III	[7135.79]†	. . .
Ca II	3933.66†	1.184
	8542.09	
Ti II	3349.41	. . .
Cr II	3132.05	. . .
Fe II	3002.65	1.086
Fe III	4419.60	1.365
	5156.11	
Fe IV	[7925.02]	[1.076]
Co II	3621.20	1.606
Co III	3151.40]	[1.548]
	3259.60	[2.002]
	3782.18	[2.097]
	4740.66	[2.281]
	6994.09	[2.473]
Co IV	[7902.03]	[1.871]
		[2.382]
Ni II	3513.99	. . .
Ni III	[7889.93]	1.001

Table C8. Strong lines in the optical and NIR at 27.4 d past explosion.

| | $t_{exp} = 27.4$ d ($\Delta t_{bol} = +9.8$ d) | |
| | 3000–10 000 Å | 1.0–2.5 μm |
Ion	λ_{air} (Å)	λ_{air} (μm)
O I	7771.94	. . .
Mg II	9218.25	1.091
Si II	4130.90	1.175
	6347.11	1.370
		1.445
Si III	4552.62	1.134
S II	5453.85	[1.032]
S III	[9530.62]	. . .
Ar II	6643.69	. . .
Ar III	[7135.79]†	. . .
Ca II	3933.66†	1.885
	8542.09	
Ti II	3349.41	. . .
Cr II	3132.05	. . .
Fe II	5169.03	1.113
Fe III	4431.02	1.365
	7265.19	
Co II	3501.71	1.606
	3621.20	1.777
		2.220
		2.361
Co III	5667.05	[1.272]
	[5888.48]†	[1.548]
		[2.002]
		[2.097]
		[2.473]
Co IV	. . .	[1.871]
Ni II	3513.99	1.878
Ni III	[7889.93]	1.001

Table C9. Strong lines in the optical and NIR at 33.2 d past explosion.

| | $t_{exp} = 33.2$ d ($\Delta t_{bol} = +15.6$ d) | |
| | 3000–10 000 Å | 1.0–2.5 μm |
Ion	λ_{air} (Å)	λ_{air} (μm)
Si II	6347.11	1.175
S II	5647.02	[1.032]
S III	[9530.62]	. . .
Ar III	[7135.79]†	. . .
Ca II	3968.47†	1.184
	8542.09	
Ti II	3349.41	. . .
Cr II	3132.05	. . .
Fe II	5169.03	1.050
	7462.41	
	7711.72	
	9997.58	
Fe III	4419.60	[1.061]
Co II	3621.20	1.136
	4160.66	1.183
	4660.63	1.350
		1.406
		1.606
		1.777
		1.886
		2.134
		2.220
		2.361
		2.460
Co III	[5888.48]†	[1.272]
		[2.002]
Co IV	. . .	[1.871]
Ni II	3513.99	1.878
Ni III	[7889.93]	. . .

Table C10. Strong lines in the optical and NIR at 44.1 d past explosion.

| | $t_{exp} = 44.1$ d ($\Delta t_{bol} = +26.6$ d) | |
| | 3000–10 000 Å | 1.0–2.5 μm |
Ion	λ_{air} (Å)	λ_{air} (μm)
Si II	6347.11	. . .
S II	[4068.60]†	[1.032]
S III	[9530.62]	. . .
Ar III	[7135.79]†	. . .
Ca II	3968.47†	1.184
	8542.09	
	8662.14	
Ti II	3372.80	. . .
Cr II	3132.05	. . .
Fe II	4351.77	1.050
	4549.47	1.261
	5169.03	
	7462.41	
	7711.72	
	9997.58	
Fe III	[4658.05]†	. . .
Co II	3621.20	1.183
	9418.11	1.406
		1.503
		1.606
		1.777
		1.886
		2.134
		2.220
		2.361
		2.460
Co III	[5888.48]†	[2.002]
Ni II	8096.75	1.312

Table C11. Strong lines in the optical and NIR at 53.4 d past explosion.

| | $t_{exp} = 53.4$ d ($\Delta t_{bol} = +35.8$ d) | |
| | 3000–10 000 Å | 1.0–2.5 μm |
Ion	λ_{air} (Å)	λ_{air} (μm)
Si II	6347.11	. . .
S II	[4068.60]†	[1.032]
S III	[9530.62]	. . .
Ar III	[7135.79]†	. . .
Ca II	3179.33	1.184
	3968.47†	
	8542.09	
Ti II	3372.80	1.463
	3759.30	
Fe II	4233.17	1.050
	4549.47	1.261
	5169.03	1.370
	7462.41	1.453
	7711.72	
	9997.58	
Fe III	[4658.05]†	. . .
Co II	3621.20	1.183
		1.606
		1.777
		1.886
		2.134
		2.220
		2.361
		2.460
Co III	[5888.48]†	[2.002]
Ni II	. . .	[1.939]

Table C12. Strong lines in the optical and NIR at 64.6 d past explosion.

| | $t_{exp} = 64.6$ d ($\Delta t_{bol} = +47.0$ d) | |
| | 3000–10 000 Å | 1.0–2.5 μm |
Ion	λ_{air} (Å)	λ_{air} (μm)
Si II	6347.11	. . .
S II	[4068.60]†	[1.032]
S III	[9068.62]	. . .
	[9530.62]	
Ar III	[7135.79]†	. . .
Ca II	3933.66†	1.184
	8542.09	
Ti II	3759.30	1.463
Cr II	3132.05	1.880
	3368.04	
	3408.76]	
Mn II	3441.99	. . .
Fe II	4233.17	1.050
	4549.47	1.261
	5169.03	1.370
	6247.56	1.453
	6456.38	
	7462.41	
	7711.72	
	9997.58	
Fe III	[4658.05]†	[2.145]
Co II	3621.20	1.183
		1.606
		1.777
		2.134
		2.220
		2.361
		2.460
Co III	[5888.48]†	[2.002]
Co IV	[3936.51]†	[1.871]
Ni II	[7377.83]†	[1.939]
Ni III	[7889.93]	. . .

Table C13. Strong lines in the optical and NIR at 71.1 d past explosion.

| | $t_{exp} = 71.1$ d ($\Delta t_{bol} = +53.5$ d) | |
| | 3000–10 000 Å | 1.0–2.5 μm |
Ion	λ_{air} (Å)	λ_{air} (μm)
Si II	6347.11	. . .
S II	[4068.60]†	[1.032]
S III	[9068.62]	. . .
	[9530.62]	
Ar III	[7135.79]†	. . .
Ca II	3933.66†	1.184
	8542.09	
Ti II	3759.30	1.463
Cr II	3132.05	1.503
	3368.04	1.880
	3408.76]	
Mn II	3441.99	. . .
Fe II	4233.17	1.050
	4549.47	1.261
	5169.03	1.370
	6247.56	1.687
	6456.38	1.840
	7462.41	
	7711.72	
	9997.58	
Fe III	[4658.05]†	[2.145]
Co II	3621.20	1.183
		1.606
		1.777
		2.134
		2.220
		2.361
		2.460
Co III	[5888.48]†	[2.002]
Co IV	[3936.51]†	[1.871]
Ni II	[7377.83]†	[1.939]
Ni III	[7889.93]	. . .

Table C14. Strong lines in the optical and NIR at 86.0 d past explosion.

| | $t_{exp} = 86.0$ d ($\Delta t_{bol} = +68.4$ d) | |
| | 3000–10 000 Å | 1.0–2.5 μm |
Ion	λ_{air} (Å)	λ_{air} (μm)
Si II	6347.11	. . .
S II	[4068.60]†	[1.032]
S III	[9068.62]	. . .
	[9530.62]	
Ar III	[7135.79]†	. . .
Ca II	3933.66†	1.184
	8542.09	
Ti II	3759.30	1.463
Cr II	3132.05	1.454
	3368.04	
	3408.76]	
	4558.65	
Mn II	3441.99	. . .
Fe I	3581.19	1.197
	3734.86	
Fe II	4233.17	1.050
	5169.03	[1.257]†
	6247.56	1.370
	6456.38	1.687
	7462.41	1.840
	7711.72	
	9997.58	
Fe III	[4658.05]†	[2.145]
Co II	3501.71	1.183
		1.606
		1.777
		2.220
		2.361
		2.460
Co III	[5888.48]†	[1.548]
	[6853.53]	[2.002]
		[2.097]
Co IV	[3936.51]†	[1.871]
	[4494.29]	
Ni II	[7377.83]†	[1.939]
Ni III	[7889.93]	. . .

Table C15. Strong lines in the optical and NIR at 104.1 d past explosion.

| | $t_{exp} = 104.1$ d ($\Delta t_{bol} = +86.5$ d) | |
| | 3000–10 000 Å | 1.0–2.5 μm |
Ion	λ_{air} (Å)	λ_{air} (μm)
S II	[4068.60]†	[1.032]
S III	[9068.62]	. . .
	[9530.62]	
Ar III	[7135.79]†	. . .
Ca II	3933.66†	1.184
	8542.09	
Ti II	3759.30	1.463
	4395.03	
Cr II	3132.05	1.763]
	3368.04	
	3408.76]	
Mn II	3441.99	. . .
Fe I	3581.19	1.197
	3734.86	
Fe II	4233.17	[1.257]†
	5169.03	[1.321]
	6247.56	1.370
	6456.38	1.687
	7462.41	1.840
	7711.72	
Fe III	[4658.05]†	[2.145]
		[2.218]
		[2.348]
Co II	3501.71	1.606
		1.777
		2.460
Co III	[5888.48]†	[1.548]
	[6853.53]	[2.002]
Co IV	[4494.29]	[1.871]
Ni II	[7411.61]	[1.939]
Ni III	[7889.93]	. . .

APPENDIX D: CONTRIBUTION OF INDIVIDUAL IONS TO THE TOTAL OPTICAL AND NEAR-INFRARED FLUX

Figs D1–D7 reveal the contribution of individual ions (bottom panels) to the full optical (left) and NIR (right) synthetic spectra of DDC15 (top panels, red line), compared to SN 2002bo (top panels, black line) at all times presented in Figs 8 and 9. Only ions that impact the flux at the >10 per cent level are shown.
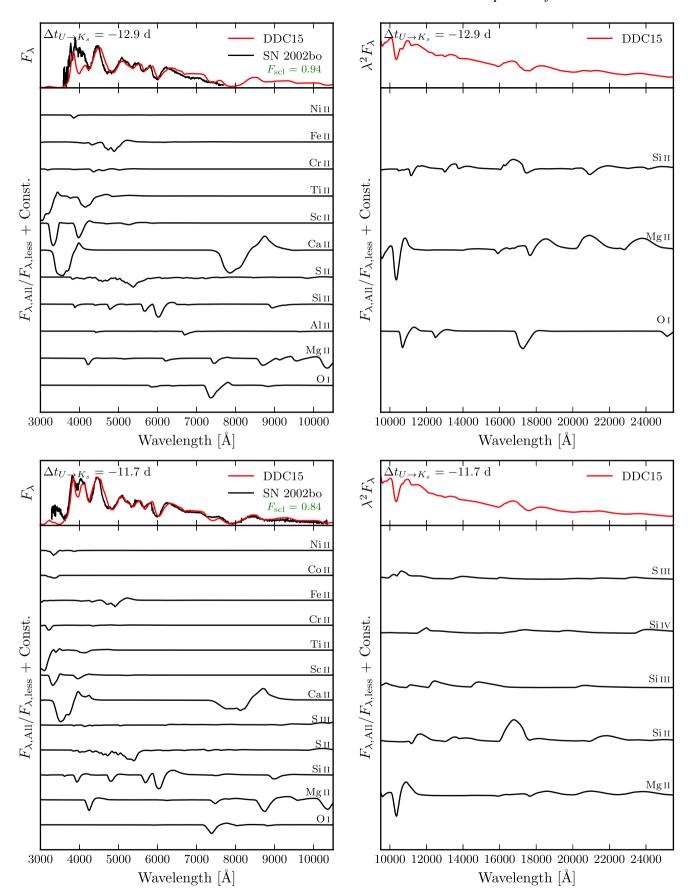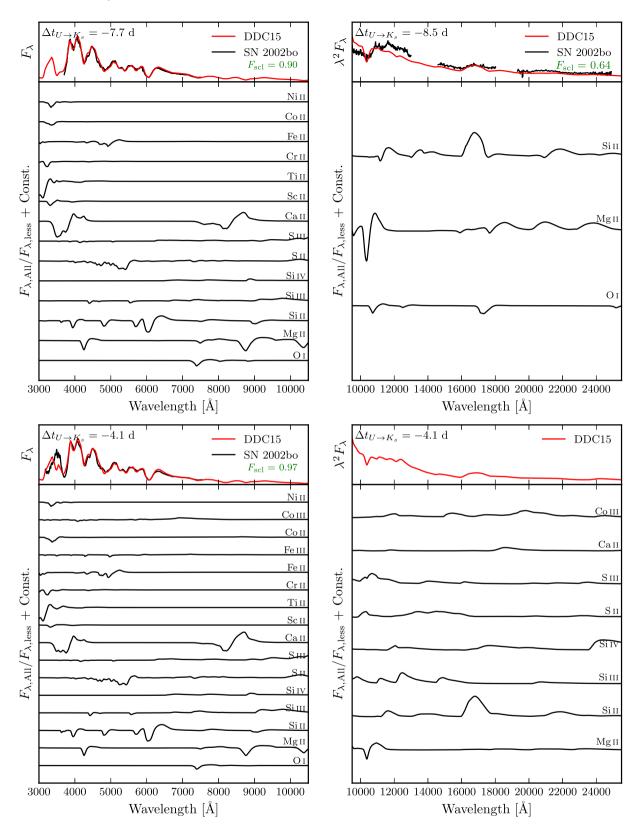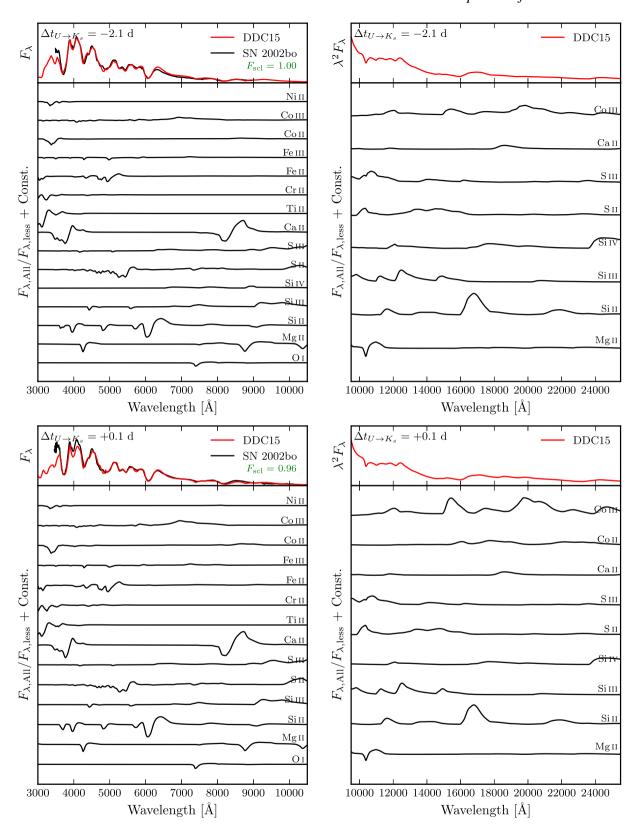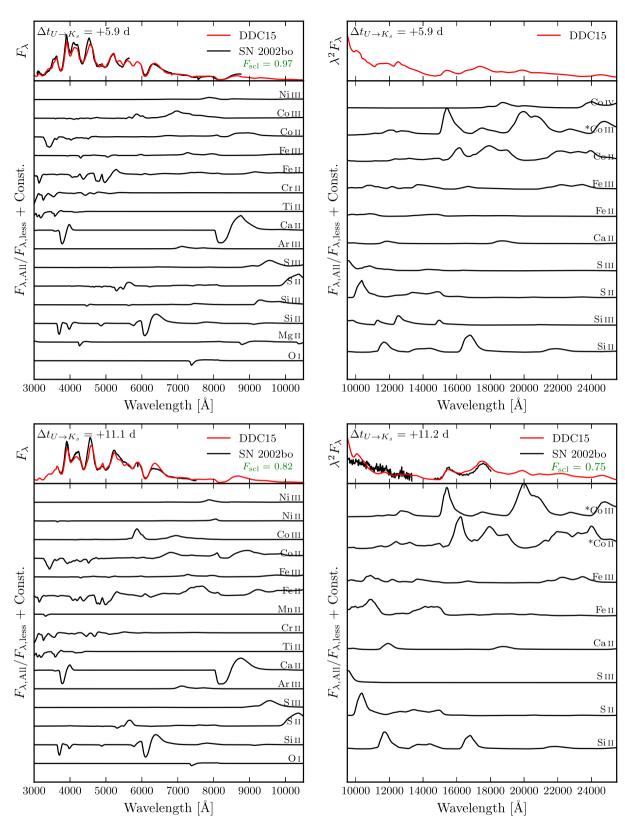
Figure D1. Contribution of individual ions (bottom panels) to the full optical (left) and NIR (right) synthetic spectra of DDC15 (top panels, red line), compared to SN 2002bo (top panels, black line) at -12.9 and -11.7 d from pseudo-bolometric ($U \rightarrow K_s$) maximum.

Figure D2. Contribution of individual ions (bottom panels) to the full optical (left) and NIR (right) synthetic spectra of DDC15 (top panels, red line), compared to SN 2002bo (top panels, black line) at −8.5 (NIR only), −7.7 (optical only), and −4.1 d from pseudo-bolometric ($U \rightarrow K_s$) maximum.

Figure D3. Contribution of individual ions (bottom panels) to the full optical (left) and NIR (right) synthetic spectra of DDC15 (top panels, red line), compared to SN 2002bo (top panels, black line) at -2.1 and $+0.1$ d from pseudo-bolometric ($U \rightarrow K_s$) maximum.

Figure D4. Contribution of individual ions (bottom panels) to the full optical (left) and NIR (right) synthetic spectra of DDC15 (top panels, red line), compared to SN 2002bo (top panels, black line) at +5.9, +11.1 (optical only), and +11.2 d (NIR only) from pseudo-bolometric ($U \rightarrow K_s$) maximum. Ion spectra marked with a '*' have been scaled down for clarity.
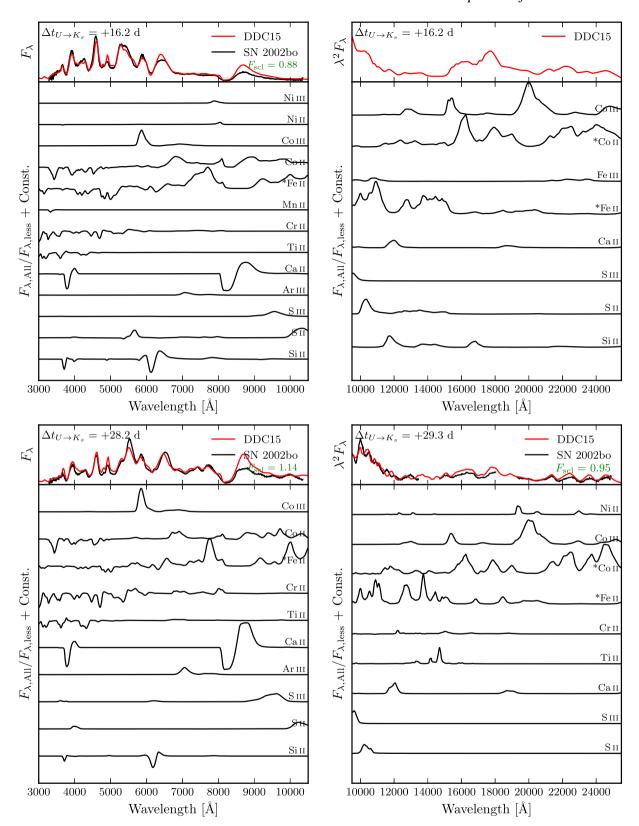
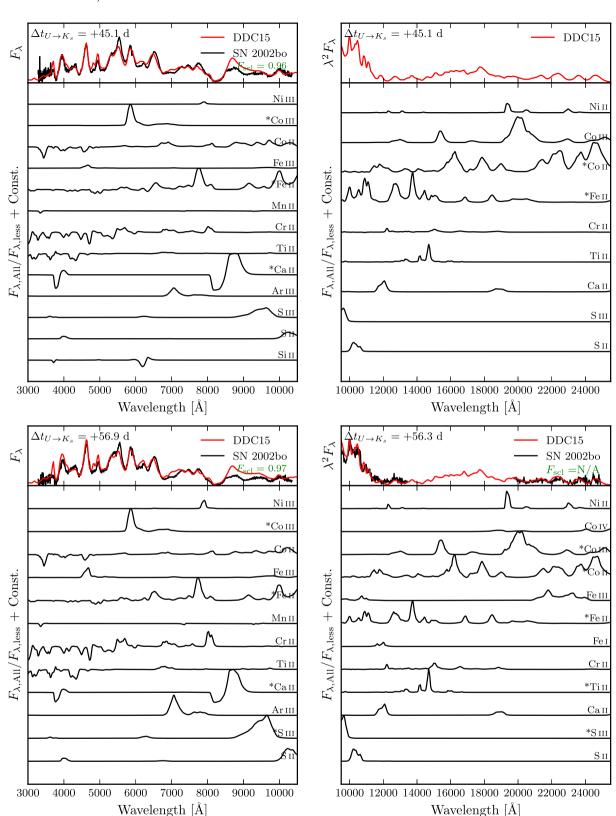**Figure D5.** Contribution of individual ions (bottom panels) to the full optical (left) and NIR (right) synthetic spectra of DDC15 (top panels, red line), compared to SN 2002bo (top panels, black line) at +16.2, +28.2 (optical only), and +29.3 d (NIR only) from pseudo-bolometric ($U \to K_s$) maximum. Ion spectra marked with a '*' have been scaled down for clarity.

Figure D6. Contribution of individual ions (bottom panels) to the full optical (left) and NIR (right) synthetic spectra of DDC15 (top panels, red line), compared to SN 2002bo (top panels, black line) at +45.1, +56.3 (NIR only), and +56.9 d (optical only) from pseudo-bolometric ($U \rightarrow K_s$) maximum. Ion spectra marked with a '*' have been scaled down for clarity.

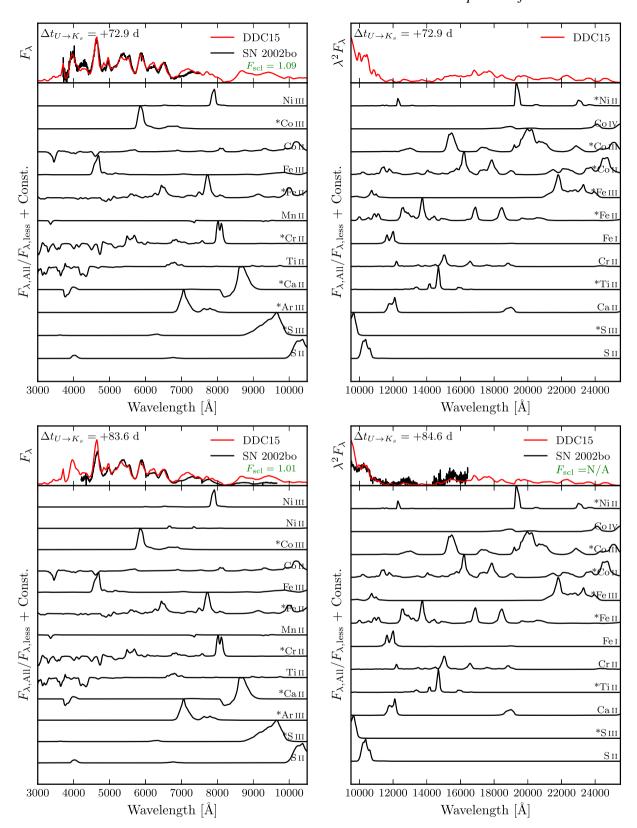**Figure D7.** Contribution of individual ions (bottom panels) to the full optical (left) and NIR (right) synthetic spectra of DDC15 (top panels, red line), compared to SN 2002bo (top panels, black line) at +72.9, +83.6 (optical only), and +84.6 d (NIR only) from pseudo-bolometric ($U \rightarrow K_s$) maximum. Ion spectra marked with a '*' have been scaled down for clarity.

This paper has been typeset from a TEX/LATEX file prepared by the author.